

C₃N₅: A Low Bandgap Semiconductor Containing an Azo-Linked Carbon Nitride Framework for Photocatalytic, Photovoltaic and Adsorbent Applications

Pawan Kumar,^{*,†} Ehsan Vahidzadeh,[†] Ujwal K. Thakur,[†] Piyush Kar,[†] Kazi M. Alam,[†] Ankur Goswami,[†] Najia Mahdi,[†] Kai Cui,[‡] Guy M. Bernard,[§] Vladimir K. Michaelis,[§] and Karthik Shankar^{*,†}

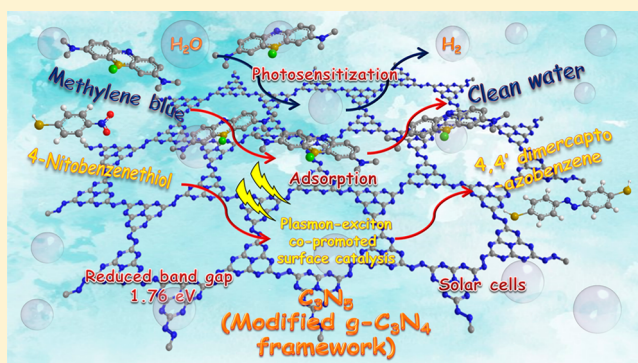
[†]Department of Electrical and Computer Engineering, University of Alberta, 9211 116 Street, Edmonton, Alberta T6G 1H9, Canada

[‡]Nanotechnology Research Centre, National Research Council of Canada, Edmonton, Alberta T6G 2M9, Canada

[§]Department of Chemistry, University of Alberta, Edmonton, Alberta T6G 2G2, Canada

Supporting Information

ABSTRACT: Modification of carbon nitride based polymeric 2D materials for tailoring their optical, electronic and chemical properties for various applications has gained significant interest. The present report demonstrates the synthesis of a novel modified carbon nitride framework with a remarkable 3:5 C:N stoichiometry (C₃N₅) and an electronic bandgap of 1.76 eV, by thermal deammoniation of melem hydrazine precursor. Characterization revealed that in C₃N₅ polymer, two *s*-heptazine units are bridged together with azo linkage, which constitutes an entirely new and different bonding fashion from *g*-C₃N₄ where three heptazine units are linked together with tertiary nitrogen. Extended conjugation due to overlap of azo nitrogens and increased electron density on heptazine nucleus due to the aromatic π network of heptazine units lead to an upward shift of the valence band maximum resulting in bandgap reduction down to 1.76 eV. XRD, He-ion imaging, HR-TEM, EELS, PL, fluorescence lifetime imaging, Raman, FTIR, TGA, KPFM etc. clearly show that the properties of C₃N₅ are distinct from pristine carbon nitride (*g*-C₃N₄). When used as an electron transport layer (ETL) in MAPbBr₃ based halide perovskite solar cells, C₃N₅ outperformed *g*-C₃N₄ in particular generating an open circuit photovoltage as high as 1.3 V, while C₃N₅ blended with MA_xFA_{1-x}Pb(I_{0.85}Br_{0.15})₃ perovskite active layer achieved a photoconversion efficiency (PCE) up to 16.7%. C₃N₅ was also shown to be an effective visible light sensitizer for TiO₂ photoanodes in photoelectrochemical water splitting. Because of its electron-rich character, the C₃N₅ material displayed instantaneous adsorption of methylene blue from aqueous solution reaching complete equilibrium within 10 min, which is significantly faster than pristine *g*-C₃N₄ and other carbon based materials. C₃N₅ coupled with plasmonic silver nanocubes promotes plasmon-exciton coinduced surface catalytic reactions reaching completion at much low laser intensity (1.0 mW) than *g*-C₃N₄, which showed sluggish performance even at high laser power (10.0 mW). The relatively narrow bandgap and 2D structure of C₃N₅ make it an interesting air-stable and temperature-resistant semiconductor for optoelectronic applications while its electron-rich character and intrasheet cavity make it an attractive supramolecular adsorbent for environmental applications.



INTRODUCTION

The last few decades have witnessed the rise of semiconducting, all-organic polymers as excellent metal-free and visible light-active materials for various optoelectronic and energy harvesting applications.¹ Although impressive improvements in performance have been achieved, particularly for plastic solar cells, the synthesis procedures for semiconducting polymers are cumbersome and difficult to scale up,² and the organic semiconductors themselves are unstable under the action of heat, light and/or ambient air.³ Consequently, there are scalability concerns related to semiconducting polymers,⁴

and requirement of heavy encapsulation to achieve even modest durability in the photovoltaic application. The same concerns, related to oxidative stability and durability, have also ruled out the use of semiconducting polymers in photocatalytic applications.

A very different approach toward forming and exploiting all-organic, polymeric semiconductors in optoelectronic and energy harvesting applications consists of using doped and

Received: January 5, 2019

Published: February 14, 2019

57 substituted graphenic frameworks as building blocks to achieve
58 two-dimensional (2D) semiconductors with well-defined
59 bandgaps and structural motifs.^{5,5,6} The major advantages of
60 graphenic semiconductors are their chemical robustness and
61 the simplicity of synthesis. Several graphenic semiconductors
62 are synthesizable using solvothermal synthesis and/or solid-
63 state reactions, and graphenic semiconductors are perfectly
64 stable in ambient conditions up to temperatures of several
65 hundred degrees Celsius. As a result of this exceptional
66 stability, almost no structural or chemical degradation of
67 photocatalytic action is observed even after several reuse
68 cycles.⁷

69 Among graphenic semiconductors, graphitic carbon nitride
70 ($g\text{-C}_3\text{N}_4$), composed of tris-*s*-triazine (*s*-heptazine, C_6N_7) units
71 bridged together with nitrogen atoms to give a 2D graphitic
72 structure has gained significant interest due to its astonishing
73 electronic, optical and physicochemical properties.⁸ Continu-
74 ous repetition of the heptazine motif leads to a bandgap of 2.7
75 eV with band edge positions (E_{CB} , -1.1 eV and E_{VB} , $+1.6$ eV)
76 that render it compatible with sunlight-driven water splitting,
77 CO_2 photoreduction and the photooxidation of a number of
78 organic compounds.⁹ Further, the plentiful presence of
79 electron-rich sites and basic nitrogens in the $g\text{-C}_3\text{N}_4$ scaffold
80 enables the promotion of various catalytic reactions, i.e.
81 alkylation, esterification, oxidation, etc. and pollutant removal
82 (dye adsorption).^{6a,10} The somewhat wide bandgap of $g\text{-C}_3\text{N}_4$
83 means that it can absorb only the ultraviolet and blue fraction
84 of solar spectrum ($\lambda < 450$ nm), which limits its performance
85 in photocatalytic and photovoltaic applications. Doping with
86 various heteroatoms such as P, F, B and S has been utilized to
87 improve the visible light absorption profile and photo-
88 efficiency.¹¹ Like all semiconductors, $g\text{-C}_3\text{N}_4$ suffers the innate
89 drawback of carrier recombination detrimental to catalytic and
90 photocatalytic processes. Many surface modification ap-
91 proaches such as increasing the surface area via soft and
92 hard templating, using two or more precursors, transformation
93 of bulk material into sheets, doping with metals (Ag, Cu, Rh,
94 Pt, Na, etc.) and metal oxides (CoO_x) for electron and hole
95 capture, coupling with other semiconductors/metal complexes
96 to form heterojunctions, and blending with graphene have
97 been employed to improve the photocatalytic and catalytic
98 performance of $g\text{-C}_3\text{N}_4$.¹² However, less attention has been
99 paid to chemical structure modification, which can lead to the
100 generation of a more robust, band edge tuned $g\text{-C}_3\text{N}_4$
101 framework with entirely new physicochemical properties for
102 efficient catalytic/photocatalytic applications. It has been
103 found that addition of extra nitrogen-rich moieties in the $g\text{-C}_3\text{N}_4$
104 scaffold to increase the N:C ratio from 4:3 ratio in CN
105 can reduce the bandgap significantly, due to a more extended
106 conjugated network and the participation of the lone pair on
107 the N atom with the π conjugated system of heptazine motif.
108 Vinu et al. demonstrated the synthesis of N-rich carbon nitride
109 (MCN-8) using 3-amino-1,2,4-triazole to afford C_3N_5
110 stoichiometry resulting in a significant decrease in bandgap
111 (2.2 eV) due to extended conjugation.¹³ However, this
112 increase in N:C ratio to 5:3 (from the 4:3 ratio in $g\text{-C}_3\text{N}_4$)
113 was due to the presence of the N-rich 1,2,4-triazole moiety
114 linked to the heptazine motif and not because of the direct
115 incorporation of the extra N atom in the heptazine nucleus.
116 The same group has also reported the synthesis of mono/and
117 diamino-*s*-triazine based carbon nitride materials (i.e., MCN-
118 ATN, MCN-4 and MCN-9) with C_3N_5 to C_3N_6 stoichiometry
119 using 3-amino-1,2,4-triazine/aminoguanidine hydrochloride

precursor and SBA-15/KIT-6 templating material.¹⁴ The N-
rich 1,2,4-triazine or 1,2,4,5-tetrazine moieties were bridged
together with tertiary nitrogen in a similar fashion to triazine
based carbon nitride and a significant decrease in band gap was
observed due to the addition of extra nitrogens. In a recent
report, mesoporous triazole and triazine framework modified
carbon nitride materials with $\text{C}_3\text{N}_{4.8}$ empirical formula
synthesized by using 5-amino-1H-tetrazole (5-ATTZ) pre-
cursor and their hybrid with graphene displayed excellent
performance in the oxygen reduction reaction.¹⁵ Fang et al.
reported the synthesis of nitrogen self-doped graphitic carbon
nitride (C_3N_{4+x}) by heating hydrazine treated melamine in a
sealed ampule. In C_3N_{4+x} the excess N atoms replace terminal
C atoms in the heptazine nucleus and the excess charge on the
N atom gets redistributed leading to electron-rich heptazine
motifs due to which C_3N_{4+x} possessed a narrower bandgap
(2.65 eV) with concomitant shifts in the conduction and
valence band edge positions (E_{CB} , -0.98 eV and E_{VB} , $+1.67$
eV).¹⁶ In these N-rich carbon nitrides, the N-rich triazine or
heptazine based unit remains linked together with tertiary
nitrogen, $\text{N}(\text{C})_3$ and increased stoichiometric N:C ratio was
due to the replacement of C via N in triazine or heptazine ring
system. Similarly, carbon-rich C_3N_4 network also facilitates
bandgap narrowing and efficient charge separation due to the
extended conjugated network. Zhang et al. reported the
hydrothermal synthesis of low bandgap, C-rich C_3N_4 materials
with extended conjugated networks using melamine (as
heptazine ring source) and glucose (as carbon source)
precursors.^{12c,17} However, the use of melamine and other C
and N sources can afford only C_3N_4 structures possessing
randomly distributed domains within the C_3N_4 framework due
to the uncontrolled reaction and these regions work as trap
centers. Melem (2,5,8-triamino-*s*-heptazine) considered the
smallest monomeric unit of $g\text{-C}_3\text{N}_4$ framework, provides the
opportunity to manipulate chemical structure by incorporating
other units in the C_3N_4 framework in a more controlled
fashion.¹⁶⁻¹⁸ Shiraiishi et al. reported the synthesis of modified
CN-polydiimide framework ($g\text{-C}_3\text{N}_4/\text{PDI}_x$) by solid-state
reaction between melem and electron deficient pyromellitic
dianhydride (PMDA) and demonstrated that the band edge
positions of $g\text{-C}_3\text{N}_4/\text{PDI}_x$ could be tuned by limiting the
number of PDI units in the framework.¹⁹ Heterostructured
($\text{C}_{\text{ring}}\text{-C}_3\text{N}_4$) embodiments of conductive, in-plane, π con-
jugated carbon rings incorporated in the C_3N_4 matrix were
prepared by thermal dehydrogenation reaction between
glucose and melem, and the obtained $\text{C}_{\text{ring}}\text{-C}_3\text{N}_4$ hetero-
structure achieved fast spatial charge transfer from $g\text{-C}_3\text{N}_4$ to
 C_{ring} motif facilitating efficient water splitting.^{18d,20} The
replacement of amino functionalities on melem/melamine by
nitrogen-rich functionalities, i.e. azide ($-\text{N}_3$), expedited the
synthesis of N-rich carbon nitride, i.e. 2,5,8-triazido-*s*-
heptazine, $(\text{C}_6\text{N}_7)(\text{N}_3)_3$, which after thermal heating, afforded
N-rich carbon nitride.^{20,21} Likewise, triazine containing N-rich
CN was also synthesized by thermal annealing of 2,4,6-
triazido-1,3,5-triazine [cyanuric triazide, $(\text{C}_3\text{N}_3)(\text{N}_3)_3$].^{20,22}
However, the synthesis procedure involved sodium azide and
concomitant shock sensitive explosion hazards; furthermore,
azide intermediates are highly undesirable.

Herein, we demonstrated the synthesis of novel modified
carbon nitride framework with a C_3N_5 stoichiometry by
thermal deamination of 2,5,8-trihydrazino-*s*-heptazine, also
known as melem hydrazine (MH), as a safe and environ-
mentally benign precursor (Figure 1). The obtained carbon

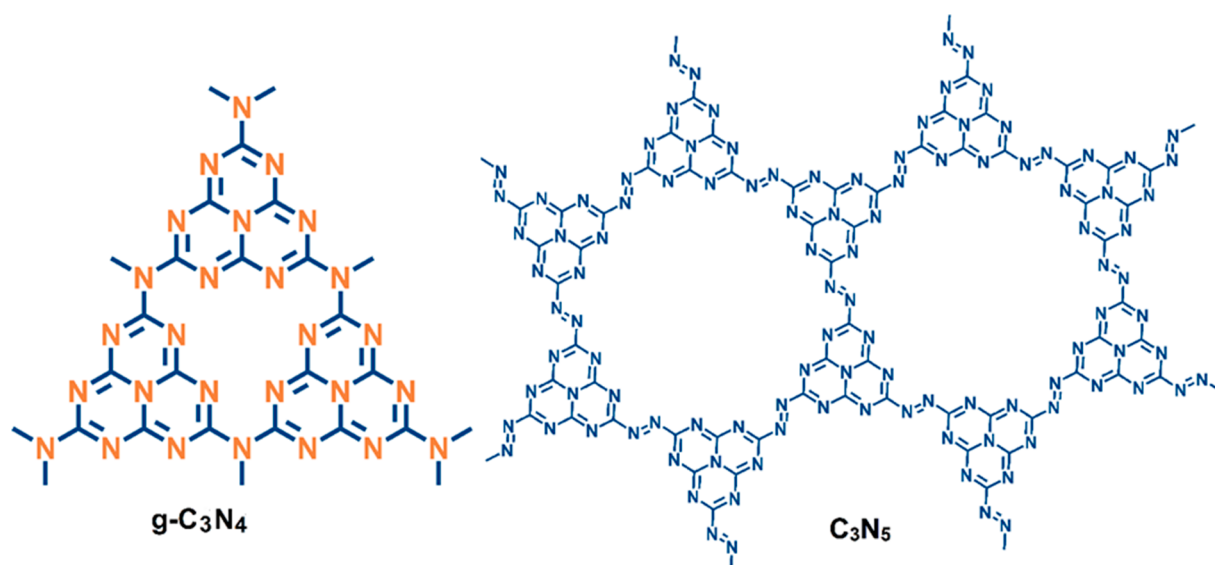


Figure 1. Chemical structure of $g\text{-C}_3\text{N}_4$ and carbon nitride modified C_3N_5 framework.

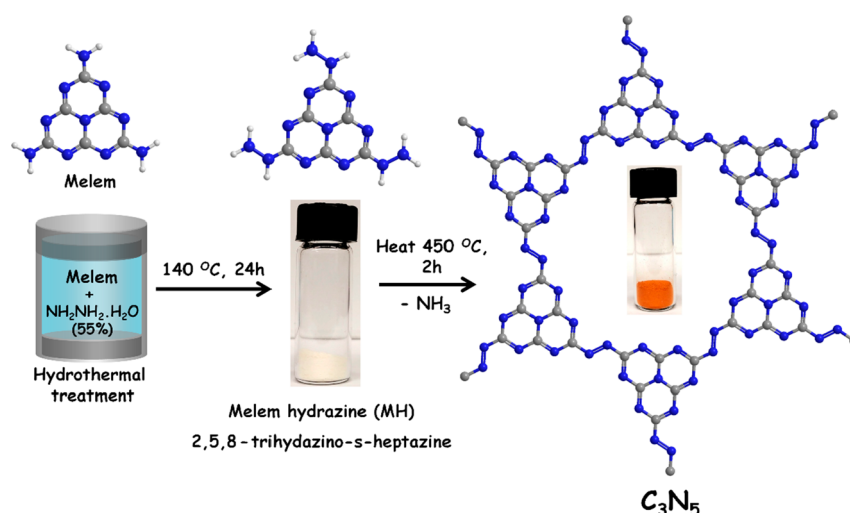


Figure 2. Synthesis schematic of C_3N_5 from melem via melem hydrazine (Atom color: N - blue, C - gray and H - white). The vials show the distinct color of the reaction product contrasted with that of the precursor.

nitride modified framework was denoted as C_3N_5 due to its 3:5 C:N stoichiometric ratio. Characterization studies revealed that the C_3N_5 framework contains heptazine moieties bridged together by azo linkage ($-\text{N}=\text{N}-$). The presence of azo linkage extends the π conjugated network due to overlap between the p orbitals on N atoms constituting the azo bond and π system of heptazine motif, which resulted in the reduction of the electronic bandgap to 1.76 eV. C_3N_5 displayed improved photosensitization properties at longer wavelengths for solar water splitting. Further, because of the increased electron charge density on the ring nitrogen, C_3N_5 exhibited instantaneous adsorption of methylene blue from aqueous solution. Solar cell devices fabricated using low bandgap C_3N_5 , as an electron transporting layer (ETL) in MAPbBr_3 based perovskite solar cells demonstrated improved power conversion efficiency (PCE), open circuit voltage (V_{oc}) etc. compared to solar cells made from $g\text{-C}_3\text{N}_4$ based ETL due to tuned band alignment. Blending a small amount of C_3N_5 (4.0 wt %) with $\text{MA}_x\text{FA}_{1-x}\text{Pb}(\text{I}_{0.85}\text{Br}_{0.15})_3$ perovskite active layer led to an increase in PCE up to 16.68% with V_{oc} of 1.065 V and J_{sc}

of 22.87 mA/cm^2 higher than conventional and $g\text{-C}_3\text{N}_4$ blended solar cell architectures. Compared to $g\text{-C}_3\text{N}_4$, C_3N_5 exhibited a remarkably enhanced performance in the plasmon-exciton codriven photoreduction of 4-nitrobenzenethiol to 4,4'-dimercaptoazobenzene.

RESULTS AND DISCUSSION

Melem (2,5,8-triamino-*s*-heptazine) served as the precursor monomeric unit for the synthesis of C_3N_5 polymer. Melem was synthesized by heating melamine at 425 °C overnight followed by purification in boiling water. The obtained melem was treated with hydrazine hydrate ($\text{NH}_2\text{NH}_2\cdot\text{H}_2\text{O}$, 55% in water) in an autoclave at 140 °C for 24 h. The treatment of melem with hydrazine hydrate transformed amino ($-\text{NH}_2$) functionalities into hydrazino ($-\text{NH}-\text{NH}_2$) functionalities, which afforded melem hydrazine, MH (2,5,8-trihydrazino-*s*-heptazine).²³ The obtained white melem hydrazine was subjected to programmed heating at 450 °C for 2 h to obtain orange colored C_3N_5 polymer (Figure 2) (see Supporting Information for experimental details). Melem hydrazine has a highly

222 hydrogen bonded structure which facilitates the formation of
 223 an azo-bridged heptazine framework by thermal condensation.
 224 Previously, Gillan also reported the formation of similar azo-
 225 bridged functionalities by heating nitrogen-rich 2,4,6-cyanuric
 226 triazide or triazido-1,3,5-triazine (C_3N_3)(N_3)₃ to form differ-
 227 ential composition triazine based carbon nitride.^{22,24} In the
 228 same report, Gillan suggested that transformation of cyanuric
 229 triazide into azo-bridged triazine carbon nitride framework
 230 proceeded through the nitrene intermediate ($C_3(N_3)_2N\cdot$) and
 231 that the formation of C_3N_5 from melem hydrazine might
 232 proceed via a similar intermediate due to the thermolabile
 233 nature of hydrazine functionalities. The structures of melem,
 234 melem hydrazine and hydrogen bonded melem hydrazine are
 235 given in Supporting Information (Figure S1).
 236 The surface morphology of the C_3N_5 polymer was
 237 investigated using a He-ion microscope equipped with an
 238 electron flood gun to facilitate positive charge neutralization
 239 accumulated from the He-ion beam (Figure 3a). The He-ion

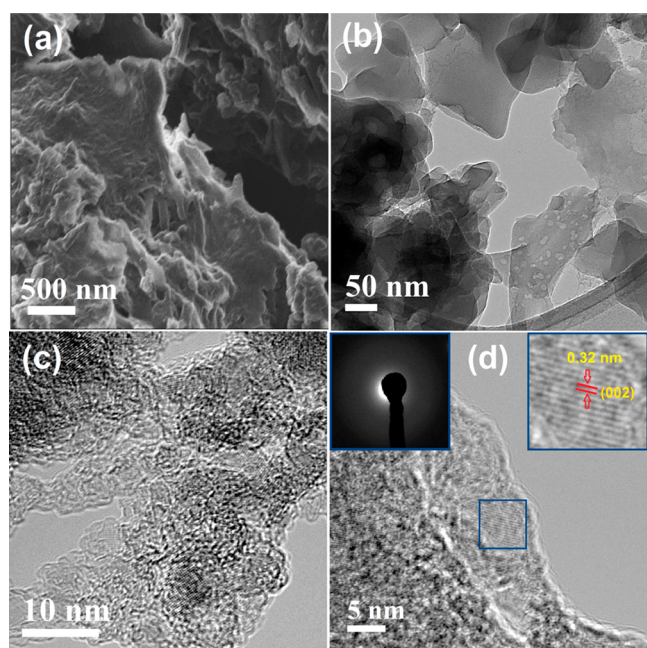


Figure 3. (a) He-ion image of C_3N_5 , and HR-TEM images of C_3N_5 (b) at 50 nm, (c) at 10 nm and (d) at 5 nm scale bar; left and right insets showing SAED diffraction pattern and interplanar d spacing, respectively.

240 images of MHP show a rough, crumpled graphenic scaffold
 241 with some erupted morphologies, which indicate that the high
 242 temperature treatment of MH monomeric unit facilitated
 243 polymerization into an irregular sheet-like structure. The fine
 244 structure of C_3N_5 material was determined using high
 245 resolution transmission electron microscopy (HR-TEM)
 246 (Figure 3b–d). The carbon nitride like layered sheet
 247 architecture is clearly evident in the TEM image of C_3N_5 at
 248 50 nm scale bar (Figure 3b). Under long duration exposure of
 249 the electron beam, C_3N_5 starts to degrade and shrink which
 250 likely resulted due to high energy electrons breaking the $-N=N-$
 251 linkage. HR-TEM images at 10 and 5 nm scale bar show
 252 crystallite fringes of nanoporous multilayered sheets with an
 253 interplanar d -spacing of 0.32 nm, corresponding to the 002
 254 plane of the graphitic structure (Figure 3c,d, and inset). The
 255 observed d -spacing in C_3N_5 was identical to $g-C_3N_4$ from

which we infer that during the thermal polymerization step, the
 256 stacking pattern of sheets in C_3N_5 remains similar to that in
 257 bulk $g-C_3N_4$. The broad, less intense ring in the selected area
 258 electron diffraction (SAED) pattern was attributed due to
 259 diffraction of electrons by the 002 plane; however, the low
 260 intensity of the ring suggests amorphous nature of the material
 261 (inset of Figure 3d).
 262

The surface chemical composition of the synthesized
 263 material was investigated using X-ray photoelectron spectroscopy,
 264 XPS (Figure 4). The XPS elemental survey scan of C_3N_5
 265 shows peaks corresponding to C 1s, N 1s, Na 1s, Cl 2p and O
 266 1s (Figure S2a). The presence of Na 1s and Cl 2p is due to
 267 intercalated Na^+ ions in the supramolecular cavity of the
 268 polymeric motif (Figure 1) and the residual NaCl formed
 269 during the purification step of MH. After excluding Na 1s, Cl
 270 2p and O 1s peaks, the at. % values of C and N in the C_3N_5
 271 were found to be 36.76% and 63.24% respectively, which
 272 represent an empirical formula of $C_3N_{5.16}$ for the C_3N_5
 273 polymer (Table 1). The obtained composition matched well
 274 with theoretical C_3N_5 (N - 62.50 at. %, and C - 37.50 at. %)
 275 stoichiometric carbon nitride materials. The high resolution
 276 XPS spectrum of C_3N_5 in C 1s region was deconvoluted into
 277 two peak components at binding energies of 284.8 and 287.9
 278 eV corresponding to the presence of sp^3 and sp^2 hybridized
 279 carbons, respectively (Figure 4a). The sp^3 carbon peak
 280 originated from adventitious carbons, edge group carbons
 281 and turbostratic carbons present in the scaffold of C_3N_5
 282 polymer while the relatively stronger sp^2 peak appeared due
 283 to $N=C-N$ type aromatic carbons, which constitute the
 284 carbon nitride-like framework of C_3N_5 .²⁵ The core level HR-
 285 XPS in N 1s after deconvolution gave two peak components
 286 located at 398.7 and 400.2 eV. The peak at a binding energy of
 287 398.7 eV was assigned to tertiary $N-(C)_3$ and secondary $C=N$
 288 $N-C$ nitrogens present in the aromatic ring structure while
 289 another peak at 400.2 eV was due to the presence of primary
 290 residual $-NH_2$ and bridging $C-N=N-C$ type nitrogens
 291 (Figure 4b).^{25,26} From the N 1s XPS spectrum, the at. % of N
 292 present in aromatic ring (N_{ring}) and bridging ($N_{bridging}$) were
 293 found to 60.47% and 39.53% respectively, and the at. % ratio
 294 obtained was 3:2, which strongly supports the proposed
 295 structure in which two heptazine units are interconnected with
 296 the azo ($-N=N-$) motif and is also consistent with the
 297 theoretical C_3N_5 azo-linked structure (Table 1). Furthermore,
 298 HR-XPS in Na 1s region gave a peak at 1071.9 eV due to the
 299 presence of Na^+ ions in the polymeric skeleton and residual
 300 NaCl (Figure S2b). The two peak components in Cl 2p XPS,
 301 at binding energy values of 198.7 and 200.2 eV ascribed to Cl
 302 $2p_{3/2}$ and Cl $2p_{1/2}$ further validated the presence of Cl^- in the
 303 form of NaCl (Figure S2c). Two XPS peaks in the O 1s region
 304 located at 531.6 and 532.4 eV were associated with surface
 305 adsorbed adventitious oxygens and $-OH$ groups (Figure S2d).
 306 The nature of C and N bonding in $g-C_3N_4$ and C_3N_5 was
 307 elucidated with electron energy loss spectroscopy (EELS)
 308 (Figure 4c,d and Figure S3). The normalized EELS spectra of
 309 $g-C_3N_4$ and C_3N_5 exhibited two major symmetric peaks due to
 310 contribution of C–K and N–K edge loss. The C K-edges
 311 signal of both $g-C_3N_4$ and C_3N_5 was composed of two peaks
 312 located at 284.6 and 293.2 eV corroborated to $1s-\pi^*$
 313 and $1s-\sigma^*$ electronic transition of sp^2 hybridized carbons
 314 trigonally coordinated with nitrogens in s -heptazine nucleus
 315 (Figure 4c).^{14a,b,27} The relative intensity of π^* C K-edge signal
 316 and π^*/σ^* peak area ratio of C_3N_5 was higher than $g-C_3N_4$
 317 suggesting increased conjugation in C_3N_5 due to extended π
 318

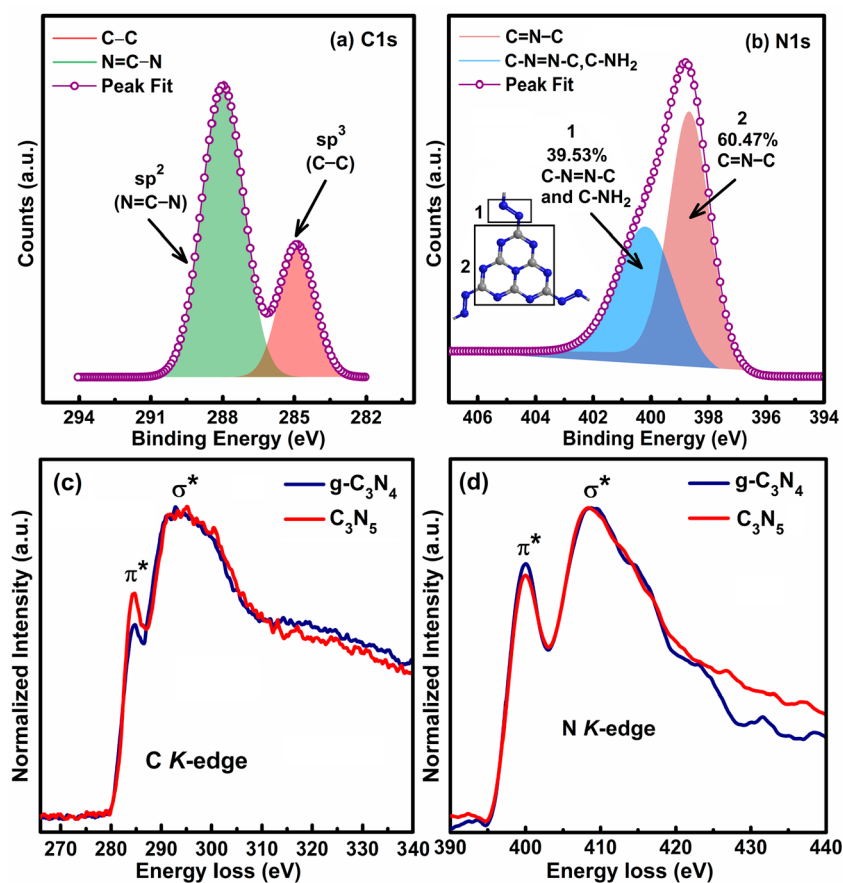


Figure 4. Core level HR-XPS spectra of C_3N_5 in (a) C 1s region, (b) N 1s region and normalized EELS spectra of $g-C_3N_4$ and C_3N_5 showing relative intensity of π^* and σ^* peaks for (c) C K-edge and (d) N K-edge loss.

Table 1. (a) Elemental Analysis of C_3N_5 Showing C, H and N wt % and Empirical Formula and (b) XPS Elemental Analysis of C_3N_5 Showing at. % and Empirical Formula and Their Comparison with Theoretical C_3N_5 Composition

(a) elemental analysis						
serial. no.		N (wt %)	C (wt %)	H (wt %)	empirical formula	$N_{\text{ring}}:N_{\text{bridging}}$ (at. % ratio)
1	CHN analysis	61.27	31.81	2.68	$C_3N_{4.95}H_{1.01}$	—
2	theoretical wt % value	66.02	33.98	—	C_3N_5	3:2 (60:40)
(b) XPS elemental analysis						
serial. no.		N (at. %)	C (at. %)	H (at. %)	empirical formula	$N_{\text{ring}}:N_{\text{bridging}}$ (at. % ratio)
3	XPS analysis	63.24	36.76	—	$C_3N_{5.16}$	~3:2 (60.47:39.53)
4	theoretical at. % value	62.50	37.50	—	C_3N_5	3:2 (60:40)

319 orbitals overlap between bridging azo functionalities and
 320 heptazine motifs.²⁸ The formation of extended π conjugated
 321 network in C_3N_5 was also supported by increased UV–vis
 322 absorption profile and shorter TRPL lifetime decay (Figures 7
 323 and 8). The N K-edges energy loss peaks for $g-C_3N_4$ and C_3N_5
 324 located at 399.8 and 408.5 eV, assigned to $1s-\pi^*$ and $1s-\sigma^*$
 325 electronic transition of sp^2 hybridized nitrogens in heptazine
 326 ring and bridging N, further verify sp^2 hybridized nitrogen-rich
 327 carbon nitride framework (Figure 4d).¹³ Absence of any new
 328 peak in N K-edge loss of C_3N_5 demonstrate bridging nitrogens
 329 in C_3N_5 have almost identical electronic environment like
 330 $N(C)_3$ nitrogens in $g-C_3N_4$.²⁹ The relative peak intensity of the
 331 N K-edge π^* signal of C_3N_5 was slightly lower than that of $g-$
 332 C_3N_4 , demonstrating enhanced contribution of azo motifs in
 333 $1s-\sigma^*$ transition. The replacement of tertiary bridging nitro-
 334 gens, $N(C)_3$ in $g-C_3N_4$ via azo nitrogens, $C-N=N-C$,
 335 renders a lone pair on azo nitrogens, which contributes to σ^*

signal and relative intensity of π^* signal suppressed. However,
 336 the total peak area of the N K-edge peak for C_3N_5 was
 337 increased, which demonstrated addition of extra nitrogens in
 338 the carbon nitride framework. The N:C atomic ratio of C_3N_5
 339 was calculated to be 1.62, which was in close agreement with
 340 the theoretical value (1.66) and C:N value obtained from
 341 CHNS analysis (1.65). Slightly lower N content might be due
 342 to cleavage of azo bond resulting in loss of some nitrogens
 343 under high energy electron beam. 344

To probe the proposed composition and structure of the
 345 synthesized C_3N_5 material, CHNS elemental analysis was
 346 performed which gave 61.27 wt % N, 31.81 wt % C and 2.68
 347 wt % H suggesting an empirical formula of $C_3N_{4.95}H_{1.01}$ which
 348 was in close proximity with the theoretical wt % for C_3N_5
 349 composition (Table 1). Slight difference between predicted
 350 and observed C:N ratio might be due to the presence of
 351 unbonded $-NH_2$ at the edge of sheets, formed by cleavage of
 352

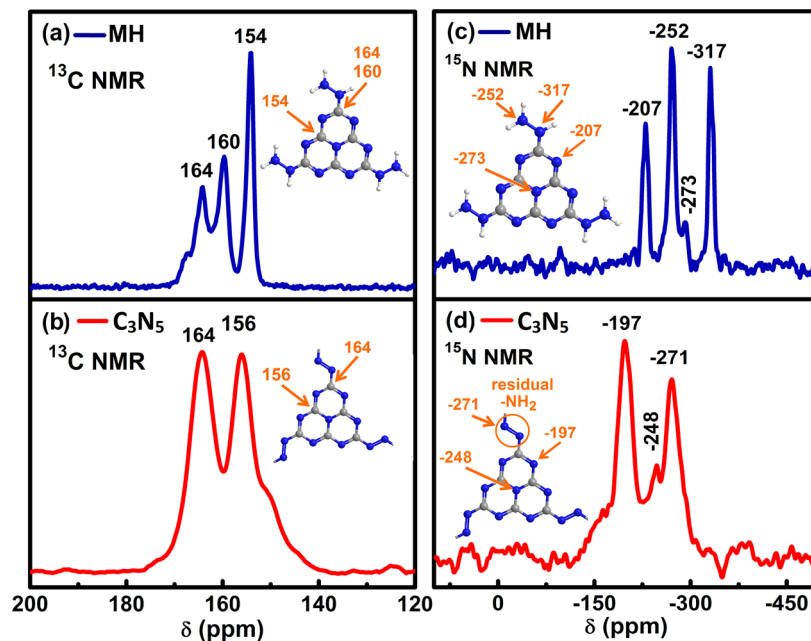


Figure 5. CPMAS NMR spectra (a) ^{13}C of MH, (b) ^{13}C of C_3N_5 , (c) ^{15}N of MH and (d) ^{15}N of C_3N_5 .

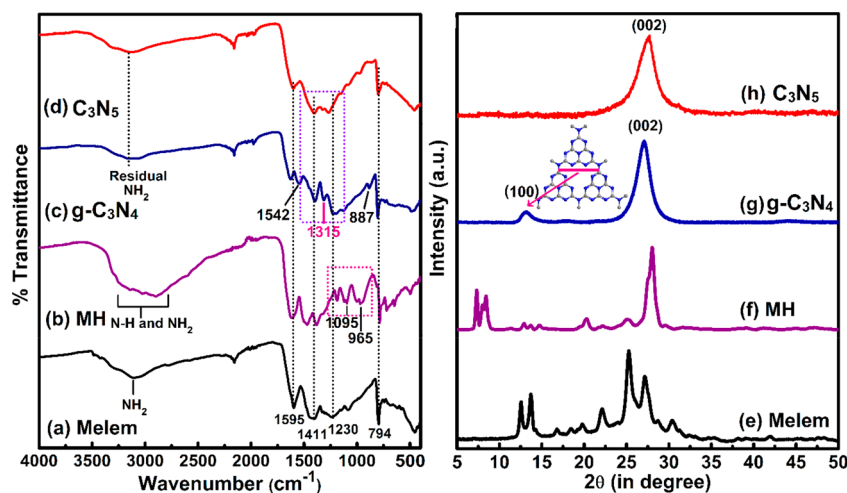


Figure 6. FTIR spectra of (a) melem, (b) melem hydrazine, (c) $\text{g-C}_3\text{N}_4$, (d) C_3N_5 , and XRD diffraction pattern of (e) melem, (f) melem hydrazine, (g) $\text{g-C}_3\text{N}_4$, (h) C_3N_5 .

353 hydrazino group ($-\text{NH}-\text{NH}_2$) at elevated temperature and
 354 loss of some azo nitrogens.^{9b,10b} As expected, sulfur was not
 355 present at measurable levels. Notably, the observed hydrogen
 356 might arise from $-\text{NH}_2$ and $-\text{OH}$ groups present at the edge
 357 of the polymeric framework.

358 To elucidate the chemical structure of MH and C_3N_5
 359 materials, solid-state nuclear magnetic resonance (NMR)
 360 spectroscopy using the cross-polarization magic-angle spinning
 361 (CPMAS) technique was performed (Figure 5). CPMAS
 362 NMR enables the structural investigation of local- and
 363 medium-range structure in micro- and nanocrystalline
 364 compounds. The ^{13}C CPMAS NMR spectra of melem
 365 hydrazine (MH) display three NMR signals at 164, 160 and
 366 154 ppm (Figure 5a). The ^{13}C NMR signals at 164 and 160
 367 ppm originated from $\text{N}_2\text{C}-\text{NHNH}_2$ carbons while the
 368 resonance at 154 ppm was observed from CN_3 carbons of
 369 the heptazine nucleus. The observed signals were in good
 370 agreement with the reported NMR spectra for MH and melem

371 based structures.^{18a,24,30} The CPMAS NMR spectrum of C_3N_5
 372 exhibits two ^{13}C NMR signals of approximately equal intensity
 373 at 164 and 156 ppm for $\text{N}_2\text{C}-\text{N}=\text{N}-$ and CN_3 carbons
 374 (Figure 5b).^{24,30,31} The $\text{N}_2\text{C}-\text{NHNH}_2$ carbon signal of MH
 375 located at 160 ppm arising due to C-H functionalities
 376 disappeared in the ^{13}C NMR of C_3N_5 , which confirms removal
 377 of $-\text{NHNH}_2$ protons and formation of an azide linkage during
 378 polymerization step agreeing with ^{15}N CPMAS NMR, *vide*
 379 *infra*. Furthermore, the appearance of equally intense (Cc:Ce/
 380 1:1.07) ^{13}C peaks in the ^{13}C NMR spectrum of C_3N_5 suggests
 381 that heptazine units are in the presence of a symmetric azo
 382 bridging motif (where Cc corresponds to central carbons in
 383 ring and Ce to external carbons bonded to azo N). A slight
 384 shift to higher frequency in CN_3 carbon peaks from 154 ppm
 385 in MH to 156 ppm in C_3N_5 suggests shielding of carbons due
 386 to N 2p overlap of azo and aromatic π system, which extends
 387 the π conjugated network.³²

388 The ^{15}N CPMAS NMR spectrum of MH exhibits four
389 signals, -207 , -252 , -273 and -317 ppm (Figure 5c).^{23a} The
390 ^{15}N NMR signal at -207 ppm and another weak signal at
391 -273 ppm were assigned to (NC_2) and (NC_3) nitrogens of the
392 heptazine motif,^{23a,31b,32,33} while the peaks at -252 and -317
393 ppm assigned to NH_2 and NH terminal nitrogens of hydrazino
394 moiety.^{35,34} The transformation of MH to C_3N_5 proceeds with
395 removal of NH_3 and formation of azo linkage which was
396 evident from the disappearance of NH_2 and NH peaks at -252
397 and -317 ppm in the ^{15}N NMR spectrum of C_3N_5 (Figure
398 5d). The two NMR peaks in the ^{15}N NMR spectra of C_3N_5 at
399 -197 and -248 (weak) ppm were attributed to NC_2 and NC_3
400 nitrogens of heptazine skeleton while another peak at -271
401 ppm arose from $-\text{N}=\text{N}-$ (and residual NHs) type nitrogens.
402 As the N atoms are in similar chemical environments, a
403 semiquantitative CPMAS NMR analysis of the ^{15}N peak areas
404 achieved by peak integration of NC_2 and NC_3 and $-\text{N}=\text{N}-$
405 resonances was found give a ratio of 1.00:0.18:0.54, which was
406 in good agreement with the theoretical value (1.00:0.17:0.5)
407 calculated for C_3N_5 polymeric structure containing heptazine
408 units interconnected with azo linkage (Figure S1). Further-
409 more, ^1H NMR of MH gave an intense peak at 5.11 ppm due
410 to NH and NH_2 hydrogens (Figure S4). This intense peak
411 disappeared in the ^1H NMR spectra of C_3N_5 further
412 confirming the removal of NH hydrogens and a very broad
413 peak centered at 9.18 ppm appeared due to intercalated
414 hydrogen, and residual carboxy and aldehyde hydrogens
415 (essential for the CPMAS approach to function whereby ^1H
416 magnetization is transferred to ^{13}C and ^{15}N). All these NMR
417 results validate the successful synthesis of a modified carbon
418 nitride framework.

419 Fourier transform infrared (FTIR) spectroscopy was
420 employed to determine the change in functional moiety in
421 the material (Figure 6a–d). The FTIR spectrum of melem
422 shows characteristic broad peaks at 3109 cm^{-1} due to the
423 combined symmetric and antisymmetric stretch vibrations of
424 $-\text{NH}_2$ and $-\text{OH}$ ($\nu_{\text{N-H}}$ and $\nu_{\text{O-H}}$) groups. The IR bands at
425 1595 , 1411 , 1230 and 1078 cm^{-1} are ascribed to the $\text{C}-\text{N}$
426 stretch ($\nu_{\text{C-N}}$) of heptazine (C_6N_7) aromatic nucleus (Figure
427 6a).^{18a,31b,34a,35} The $\text{N}-\text{H}$ stretch band ranging from 3153 to
428 2895 cm^{-1} for MH was found to become broader due to
429 combinational symmetric and asymmetric $\text{N}-\text{H}$ stretches of
430 $-\text{NH}-\text{NH}_2$ group in MH, which confirms the successful
431 transformation of $-\text{NH}_2$ moiety in melem to $-\text{NH}-\text{NH}_2$ in
432 melem hydrazine (Figure 6b). The broadening of the NH peak
433 was attributed to strong intermolecular hydrogen bonding in
434 MH molecules.^{35,36} However, all stretching and bending peaks
435 due to heptazine aromatic ring skeleton remain preserved,
436 which indicates that the heptazine motif remains unchanged
437 during the hydrazine treatment. Additionally, some new peaks
438 emerged at 1095 and 965 cm^{-1} implicating the $\text{N}-\text{N}$ stretch
439 and $-\text{NH}_2$ rocking vibration, respectively.^{18a,36,37} Graphitic
440 carbon nitride shows characteristic peaks at 3145 cm^{-1} due to
441 residual $-\text{NH}_2$ and $-\text{OH}$ stretch and $1639-1145\text{ cm}^{-1}$ due to
442 triazine ring stretch and 798 cm^{-1} for triazine ring bending
443 vibration was in good agreement with the reported literature
444 (Figure 6c).^{37,38} After conversion of MH to C_3N_5 by thermal
445 annealing, the intensity of $-\text{NH}-\text{NH}_2$ peak of MH was
446 diminished which implicated the transformation of $-\text{NH}-$
447 NH_2 group into azo ($-\text{N}=\text{N}-$) linkage through the removal
448 of NH_3 (Figure 6d). It is important to note that vibration of
449 symmetrical $-\text{N}=\text{N}-$ azo linkage is forbidden due to which
450 no new sharp peak due to azo functionalities was observed.

The possibility of $-\text{NH}-\text{NH}-$ bond can be neglected due to
451 the absence of any strong $\text{N}-\text{H}$ band; however, very weak
452 broad peaks arise due to some residual $-\text{NH}_2$ present at the
453 edge of the polymeric framework. This fact was well supported
454 by CHNS analysis, which showed the presence of only one H
455 for each stoichiometric C_3N_5 unit (Table 1). Further, other
456 peaks of MH at 1095 and 965 cm^{-1} due to $\text{N}-\text{N}$ stretch and
457 $-\text{NH}_2$ rocking vibration disappear in C_3N_5 , which confirmed
458 the transformation of hydrazine group into azo moiety. Peaks
459 corresponding to the C_3N_4 framework at 1542 , 1315 and 887
460 cm^{-1} were absent in C_3N_5 , which suggests an entirely different
461 network of C_3N_5 in comparison to $\text{g-C}_3\text{N}_4$.
462

The changes in phase structure and crystalline nature of
463 melem, MH, $\text{g-C}_3\text{N}_4$ and C_3N_5 were investigated through the
464 measurement of X-ray diffraction (XRD) (Figure 6). The XRD
465 pattern of melem demonstrated a series of peaks located at
466 12.5° , 13.6° , 16.7° , 18.4° , 19.7° , 22.0° , 25.2° , 27.2° and 30.4° ,
467 in close agreement with previous reports (Figure 6e).^{38,39} The
468 XRD results indicate the absence of any melamine impurity in
469 the melem sample.^{18b,39a} Because of the transformation of
470 melem into melem hydrazine, the XRD pattern of MH
471 changed, with new peaks being observed at 2θ values of 7.3° ,
472 7.9° , 8.4° , 12.9° , 13.7° , 14.8° , 25.1° and 28.0° (Figure 6f). Bulk
473 $\text{g-C}_3\text{N}_4$ shows two distinct XRD peaks at 2θ values of 27.1°
474 and 13.0° indexed to the 002 and 100 planes of carbon nitride
475 materials (Figure 6g). The 002 peak with a 0.32 nm interplanar
476 d spacing was correlated to interplanar stacking of sheets while
477 100 peaks with a 0.68 nm spacing was specific to in-plane
478 structural packing of heptazine units (Figure 6g).^{18b,39b,40} The
479 XRD pattern of C_3N_5 exhibits one broad 002 peak at 27.6°
480 corresponded to 0.33 nm interplanar sheet distance. The slight
481 increase in 2θ value and d spacing can be explained due to
482 repulsion between electron-rich π conjugated C_3N_5 sheets as in
483 graphite (0.34 nm) (Figure 6h). Further, the absence of 100
484 peak, a specific feature of in-plane packing, suggests distortion
485 in the carbon nitride framework and broadening of the
486 nanochannel distance between heptazine units due to azo
487 ($-\text{N}=\text{N}-$) bridging linkage, further consistent with ^{13}C and
488 ^{15}N NMR resonance broadening above, suggesting local/
489 medium-range disorder. Also, bridging of two heptazine units
490 with two nitrogens through in-plane lattice packing is less
491 efficient in C_3N_5 which was responsible for the absence of any
492 expected peak at lower 2θ values. These XRD results clearly
493 support the distinct structure of C_3N_5 possessing azo linkage.

Raman spectra of melem acquired using 632 nm laser
495 excitation show characteristic fingerprint peaks of melem at 435
496 and 697 cm^{-1} due to heptazine ring (C_6N_7) breathing modes
497 and a broad hump at 1452 cm^{-1} due to $-\text{NH}_2$ bending mode
498 (Figure S5a).^{18a,40a} Raman spectra of MH demonstrate many
499 signature peaks correlated to the core at 472 , 744 and 1529
500 cm^{-1} , which were shifted in comparison to melem due to
501 functionalization while other peaks due to various vibrations of
502 the heptazine nucleus and hydrazine group were observed at
503 127 , 342 , 537 , 985 , 1159 , 1314 and 3071 cm^{-1} , in good
504 agreement with the reported literature (Figure S5b).^{18a,23a,40b,41} The Raman spectra of $\text{g-C}_3\text{N}_4$ display many
505 prominent peaks due to the heptazine framework at 471 , 697
506 and 706 cm^{-1} (heptazine ring breathing modes) and two
507 additional peaks at 1233 and 1567 cm^{-1} corresponding to the
508 $-\text{NH}_2$ bending mode and graphitic G band (Figure S5c).^{23a,42}
509 Further, the presence of a broad hump extended from 1100 to
510 1600 cm^{-1} suggests multilayer stacking of $\text{g-C}_3\text{N}_4$ sheets.^{41,43}
511 In the Raman spectra of C_3N_5 , only trace peaks of melem
512

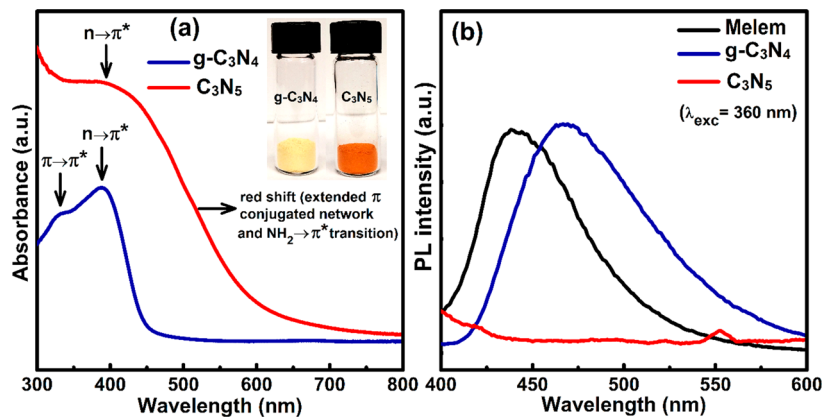


Figure 7. (a) DR-UV-vis spectra of g-C₃N₄ (blue) and C₃N₅ (red), with inset showing photographs of g-C₃N₄ and C₃N₅ samples and (b) Steady-state PL spectra of melem (black), g-C₃N₄ (blue) and C₃N₅ (red) obtained using an excitation wavelength of 360 nm.

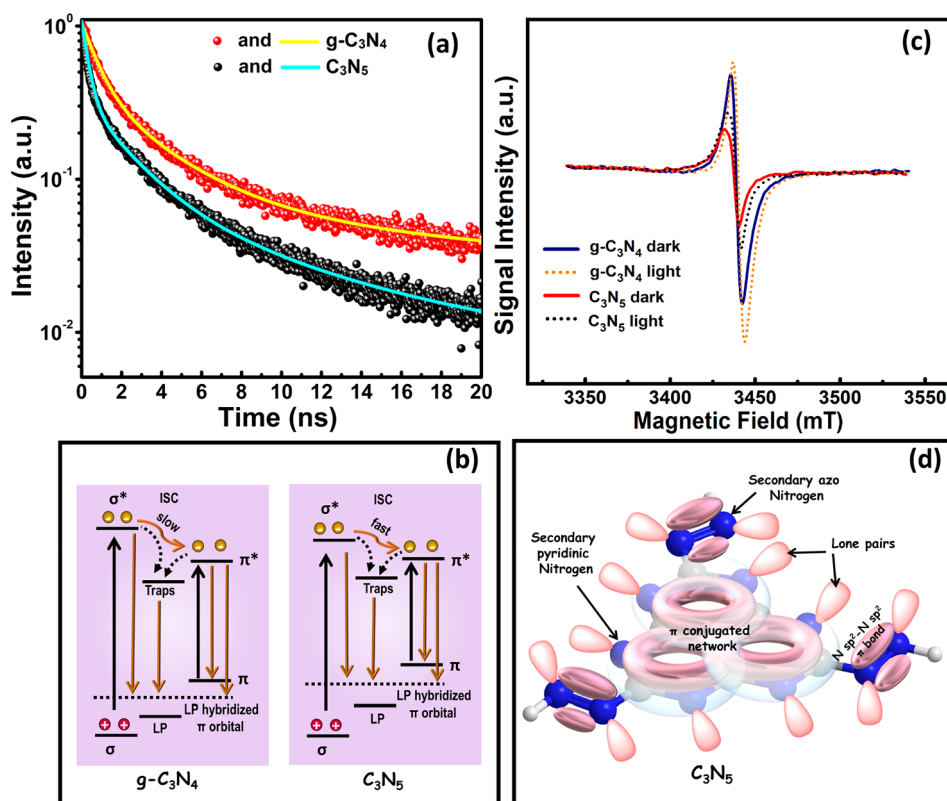


Figure 8. (a) PL lifetime decay curves of g-C₃N₄ (red; triexponential fit, yellow line) and C₃N₅ (black; triexponential fit, cyan), (b) Schematics of various energy levels bands and possible route of charge carriers recombination (c) X-band EPR spectra of g-C₃N₄ in the dark (blue), after light irradiation (orange dots) and C₃N₅ in the dark (red) and after light irradiation (black dots) at room temperature, (d) Plausible molecular orbital overlap representation of C₃N₅.

514 hydrazine motif are observed which indicates the complete
515 transformation of MH to C₃N₅. Two small peaks were
516 observed at 1085 and 1161 cm⁻¹ due to the mixed vibration of
517 heptazine motif and azo stretch (Figure S5d). A sharp peak at
518 1609 cm⁻¹ originated due to the C=N stretching mode.

519 **Figure 7a** displays the diffuse reflectance UV-vis (DR-UV-
520 vis) spectra of g-C₃N₄ and C₃N₅. The DR-UV-vis spectra of g-
521 C₃N₄ shows a characteristic absorption peak between 200 and
522 400 nm with a band tail extended up to 450 nm due to charge
523 transfer from the populated valence band of the nitrogen atom
524 (2p orbitals) to the conduction band of the carbon atom (2p
525 orbitals) of carbon nitride. The less intense absorption band at

330 nm is due to $\pi \rightarrow \pi^*$ transition in the conjugated network
526 while another intense peak at ca. 387 nm appeared due to $n \rightarrow$
527 π^* transition from nitrogen nonbonding orbital to the aromatic
528 nonbonding orbital.^{12b,42-44} The DR-UV-vis spectrum of
529 C₃N₅ demonstrates a drastic change in the UV-vis absorption
530 profile in comparison to g-C₃N₄ due to a more extended π
531 conjugated network (Figure 7a).^{12b,45} A broad absorption peak
532 around 393 nm in UV-vis spectrum of C₃N₅ was attributed to
533 $n \rightarrow \pi^*$ transition from nitrogen nonbonding orbital to the π
534 conjugated nonbonding orbital. The absorption spectrum of
535 C₃N₅ was red-shifted showing band tailing up to 670 nm, due
536 to an extended π conjugated network arising from the overlap
537

538 between N 2p orbitals of bridging azo moieties and N 2p in
539 heptazine π conjugated system. Further residual $-\text{NH}_2$ also
540 contributes to the delocalized aromatic π conjugated system.
541 Because of this, the position of the valence band gets upshifted
542 and $\pi \rightarrow \pi^*$ transition occurs at relatively low energy which
543 facilitates the absorption of a large fraction of the visible
544 spectrum and results in the sample displaying an orange color.
545 Further, the optical bandgaps of g- C_3N_4 and C_3N_5 were
546 determined using a Tauc plot by plotting a graph between
547 $(\alpha h\nu)^{1/2}$ vs $h\nu$ and extrapolation of the linear tangent to
548 abscissa; where α is absorption coefficient, h is plank constant
549 and ν is light frequency (Figure S6a). From the Tauc plot, the
550 value of bandgap for g- C_3N_4 was estimated to be 2.65 eV
551 corresponding to a band-edge at a wavelength of 467 nm, in
552 good agreement with the bandgap values reported in the
553 literature.⁴⁶ The bandgap value of C_3N_5 was calculated to be
554 1.76 eV corresponding to a band-edge at a wavelength of 707
555 nm.

556 Photoluminescence (PL) spectra were collected by exciting
557 samples using 360 nm photons to probe radiative recombina-
558 tion (Figure 7b). The PL spectrum of melem consists of an
559 intense emission peak centered at 441 nm, which is indicative
560 of radiative recombination of carriers within the melem
561 unit.^{39a,44} It is important to note here that melem exhibits
562 excitation wavelength-dependent PL emission. On the other
563 hand, g- C_3N_4 showed a sharp emission peak at 468 nm, which
564 did not shift upon changing the excitation wavelength. This
565 peak is attributed to fast interlayer carrier recombination in
566 multilayered sheets of bulk g- C_3N_4 .^{45,47} Surprisingly, C_3N_5
567 does not exhibit any distinguishing PL peak, which might be
568 indicative of efficient charge separation between the bulk and
569 the surface. Such charge transfer excitonic states involving the
570 bulk and the surface have also been observed in other
571 conjugated organic semiconductors that possess an extended
572 π -conjugated network that prevents radiative recombination by
573 delocalizing the Frenkel exciton. However, because of
574 conductive conjugated surface, nonradiative charge recombina-
575 tion can take place over new localized states in the sheets
576 scaffold.⁴⁸

577 In order to investigate the lifetime of excited charged
578 species, and charge separation processes, we collected time-
579 resolved photoluminescence (TRPL) spectra of g- C_3N_4 and
580 C_3N_5 using a single photon picosecond pulsed laser at a
581 wavelength of 405 nm. Figure 8 displays the PL lifetime decay
582 curves of g- C_3N_4 and C_3N_5 . The PL decay curve was fitted
583 triexponentially using the following equation:

$$584 \quad I(t) = A_1 e^{-t/\tau_1} + A_2 e^{-t/\tau_2} + A_3 e^{-t/\tau_3} \quad (1)$$

585 where, A_1 , A_2 and A_3 represent the normalized amplitudes of
586 each decay component and τ_1 , τ_2 and τ_3 are values of the
587 lifetime components, respectively. The existence of three
588 radiative lifetimes in the fitted PL lifetime spectra of g- C_3N_4
589 and C_3N_5 was in good agreement with previously reported
590 carbon nitride based materials.⁴⁹ The obtained values of
591 lifetimes and their fractional components are given in Table 2.

592 The three components in the PL lifetime decay curve of g-
593 C_3N_4 can be assigned to various energy states in g- C_3N_4
594 formed by the overlap of C and N sp^2 and sp^3 hybridized
595 orbitals and the presence of lone pairs of electrons, which allow
596 for various radiative transitions. g- C_3N_4 is composed of tri-*s*-
597 triazine (C_6N_7) units interconnected with tertiary nitrogen
598 atoms where C-N sp^3 hybridized state constitute high energy
599 σ and σ^* molecular orbitals while C-N sp^2 hybridization gives

Table 2. PL Lifetime of Photogenerated Charge Carrier and Their Relative Contribution in g- C_3N_4 and C_3N_5

sample	τ_1 (ns) [A ₁]	τ_2 (ns) [A ₁]	τ_3 (ns) [A ₁]	average lifetime (τ_{avg} ns)
g- C_3N_4	3.31 [0.34]	0.75 [0.63]	25.02 [0.05]	12.43
C_3N_5	8.10 [0.07]	2.11 [0.26]	0.28 [0.73]	4.40

rise to a conjugated network resulting in low energy π bonding 600
and π^* antibonding orbital, which constitutes the valence and 601
conduction bands, respectively.⁵⁰ The presence of unbonded 602
lone pairs of electrons on pyridinic N atoms creates energy 603
levels just below the π bonding orbital and their overlap with 604
the π conjugated system can further decrease the energy of the 605
 π molecular orbital resulting in the reduction of the bandgap.⁵¹ 606
The first two shorter lifetime components of 3.31 and 0.75 ns 607
with 34% and 63% contribution in g- C_3N_4 correspond to 608
charge carrier recombination from σ^* and π^* antibonding to π 609
MO.⁵² The third longer lifetime component of 25.02 ns with a 610
relative low contribution originated due to intersystem crossing 611
(ISC) of electron from σ^* and π^* orbital followed by radiative 612
relaxation to conjugated π orbital and trap-assisted radiative 613
recombination.⁵³ The first two lifetimes of C_3N_5 at 8.10 and 614
2.11 ns with 7% and 26% contributions in the PL decay curve 615
were significantly longer lived in comparison to g- C_3N_4 , 616
strongly suggesting that the introduction of azo moiety extends 617
 π conjugated network which facilitates better charge carrier 618
mobility on C_3N_5 sheets (delocalized the exciton, as 619
mentioned previously) and prevents faster charge carrier 620
recombination.⁵⁴ Further, because of extended conjugation, 621
the difference between σ^* and π^* band gets decreased, which 622
is also evident in Mott-Schottky measurement (Figure 623
S6b).^{51a} The low energy difference between σ^* and π^* 624
accelerates the transfer of electrons from σ^* and π^* orbital via 625
intersystem crossing followed by radiative relaxation, which 626
was evident from higher percentage contribution of the third 627
lifetime component (73%). 628

The average lifetime (τ_{avg}), which is regarded as coherent 629
measure to evaluate the rate of spontaneous emission, was 630
calculated from the three lifetime components using the 631
following expression: 632

$$\tau_{\text{avg}} = (A_1\tau_1^2 + A_2\tau_2^2 + A_3\tau_3^2)/(A_1\tau_1 + A_2\tau_2 + A_3\tau_3) \quad (2) \quad 633$$

From eq 2, the average lifetimes of g- C_3N_4 and C_3N_5 were 634
calculated to be 12.43 and 4.40 ns, respectively. The decreased 635
lifetime of the C_3N_5 in comparison to g- C_3N_4 coupled with the 636
very weak photoluminescence of C_3N_5 (as shown in Figure 7b) 637
is indicative of fast quenching of the C_3N_5 luminescence. The 638
fast quenching might originate from improved charge 639
separation in C_3N_5 due to a larger conjugated π network but 640
might also be due to stronger nonradiative transitions. Fast 641
exciton dissociation with concomitant high carrier mobility can 642
result in photogenerated electrons finding trap sites (and 643
moving to them) and recombining by nonradiative proc- 644
esses.^{48a} The aforementioned processes are highly likely in 645
 C_3N_5 since the presence of azo bonds extends the π network 646
because of overlap of N 2p orbital on azo nitrogens with the π 647
network of heptazine motif due to which electrons can move 648
within C_3N_5 scaffold freely. The lower PL lifetime of C_3N_5 in 649
comparison to g- C_3N_4 was consistent with steady-state PL 650
where C_3N_5 shows prodigious quenching in its PL spectrum. 651

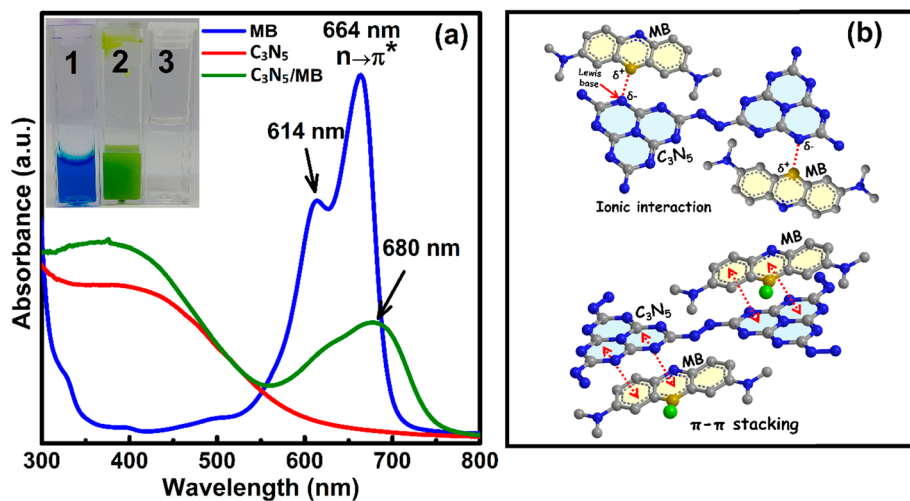


Figure 9. (a) UV-vis absorption spectra of MB (blue), C_3N_5 (red) and C_3N_5/MB solution just after 1 min of absorption (green). Inset shows photographs of (1) MB before absorption, (2) after absorption and (3) solution after centrifugation. (b) Possible ionic and π - π stacking interaction between methylene blue and C_3N_5 .

652 Electron paramagnetic resonance (EPR) spectra of $g-C_3N_4$
 653 and C_3N_5 to elucidate electronic nature and band excited
 654 paramagnetic species were collected under dark and UV
 655 irradiation at room temperature (Figure 8b). The EPR spectra
 656 of $g-C_3N_4$ under dark conditions exhibits an intense Lorentzian
 657 EPR resonance signal located at a g -factor of 2.003. The
 658 observed EPR signal originated due to the presence of
 659 unpaired electrons in the sp_2 hybridized aromatic π -system
 660 which was in good agreement with previous reports.^{36,55} The
 661 EPR signal intensity of $g-C_3N_4$ increased after UV irradiation,
 662 attributed to populated unpaired electrons in the conduction
 663 band due to π - π^* and N nonbonding to π^* (n - π^*) transition
 664 followed by slow relaxation via ISC. The observed EPR signal
 665 of C_3N_5 was also observed at 2.003 g -value, which implies basic
 666 graphitic heptazine skeleton remains intact in C_3N_5 frame-
 667 work.⁵⁶ Further, after irradiation with UV light, the EPR signal
 668 intensity of C_3N_5 was also enhanced due to increased numbers
 669 of unpaired electrons in the conduction band. However, the
 670 overall EPR signal intensity of C_3N_5 in both the dark and
 671 under UV illumination was significantly weaker in comparison
 672 to $g-C_3N_4$, which was attributed to a lesser number of unpaired
 673 electrons in C_3N_5 , which in turn can be taken as evidence of
 674 the presence of extra N atoms outside the heptazine nucleus in
 675 comparison to conventional N-rich carbon nitride materials
 676 where N atoms substitute C atoms in the heptazine motif. It is
 677 well documented in the literature that substitution of sp^2
 678 hybridized +4 state C atom in heptazine motif with sp^2
 679 hybridized +3 state N atom will liberate extra electrons in
 680 the aromatic system, which will distort electronic symme-
 681 try^{16,47,57} and also increase EPR signal intensity. However, in
 682 the case of C_3N_5 , the additional N atom makes an azo bond
 683 with an N atom outside the ring via π overlap and the extra
 684 electrons remain in the form of lone pairs (Figure 8d).
 685 Fluorescence lifetime imaging microscopy (FLIM) of
 686 samples at different spots was used to probe the homogeneity
 687 of samples and to determine the nature of the fluorescence
 688 (Figure S7). The PL spectra of $g-C_3N_4$ samples obtained from
 689 different spots exhibited identical emission profiles with a
 690 sharp intense peak at 480 nm, which was in good agreement
 691 with the steady-state PL spectrum (Figure 7b). The slight red
 692 shift in the emission peak (Figure S7a) is attributed to the

693 difference in the mechanism of excitation (750 nm two-photon
 694 excitation source for FLIM, 360 nm single photon excitation in
 695 Figure 7b). Furthermore, the emission spectrum of C_3N_5
 696 displays two relatively weak peaks centered around 410 and
 697 490 nm which likely originated from some relatively smaller
 698 C_3N_5 polymeric fragments and heptazine networks (Figure
 699 S7c). The smaller fragments are consistent with a lesser
 700 number of MH units and therefore exhibit PL properties closer
 701 to melem. FLIM images of $g-C_3N_4$ were brighter than C_3N_5
 702 which further supports our inference that the charge separation
 703 process was dominant in C_3N_5 samples (Figure S7b,d). The
 704 C_3N_5/MB samples obtained after methylene blue (MB) dye
 705 adsorption displayed relatively strong PL and brighter FLIM
 706 images due to the presence of MB in the composite (Figure
 707 S7e,f). The absence of PL quenching in the C_3N_5/MB
 708 composite further suggests the absence of photoinduced
 709 charge transfer between the methylene blue and C_3N_5 .

710 The synthesized C_3N_5 material was explored for dye
 711 adsorption studies using methylene blue (MB) as a model
 712 dye. Methylene blue is a staining dye widely used in the paper,
 713 textile and leather industries which also constitutes a good
 714 example of a colored water contaminant, which due to its
 715 excellent visible light absorption, reduces light penetration in
 716 aqueous ambients and adversely affects aquatic flora and fauna.
 717 All dye adsorption studies were carried out at room
 718 temperature and under dark conditions. UV-vis spectra of
 719 samples were collected for determining the concentration of
 720 MB solutions during dye adsorption experiments (for
 721 experimental details, see Supporting Information). MB has a
 722 sharp peak at 664 nm due to π - π^* transition and a shoulder
 723 around 614 nm which represents MB present in dimeric and
 724 polymeric π stacked forms in water (Figure 9a). After the
 725 addition of C_3N_5 sample into methylene blue solution, the
 726 color of the solution instantaneously turned green. The green
 727 solution after centrifugation turned completely colorless, which
 728 demonstrated the prompt adsorption of MB dye over the
 729 surface of C_3N_5 and subsequent settling of the MB adsorbed
 730 C_3N_5 during centrifugation. The obtained solid after
 731 centrifugation (denoted as C_3N_5/MB) exhibits a sharp
 732 absorption peak intermediate between C_3N_5 and MB with a
 733 broad peak centered at 680 nm. The redshifting in the peak of

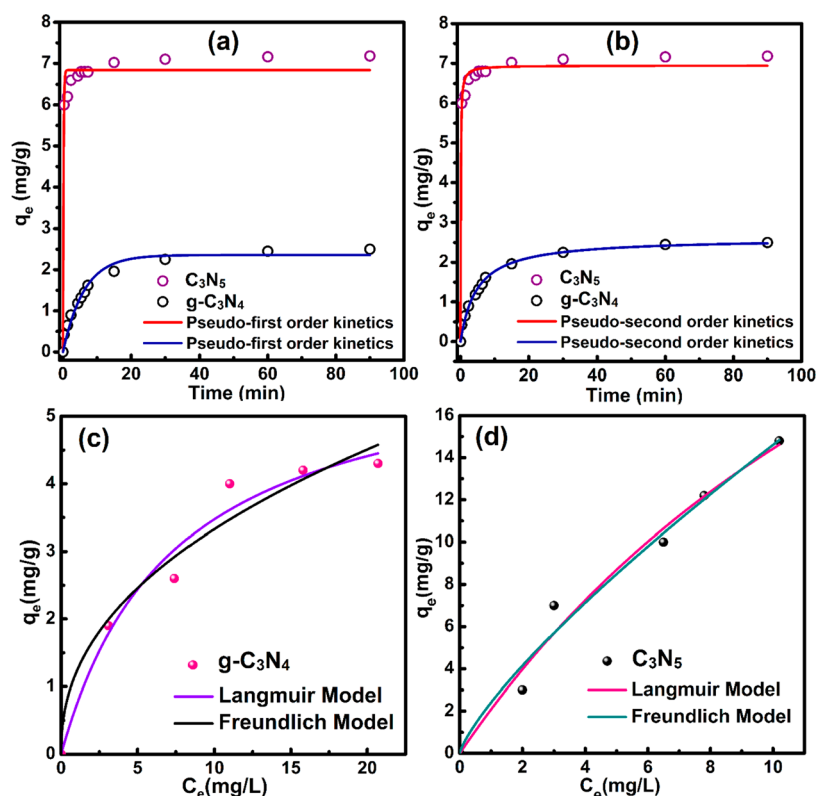


Figure 10. Kinetics of MB dye adsorption on g-C₃N₄ and MB displaying (a) pseudo-first-order fitted curve, (b) pseudo-second-order fitted curve and MB adsorption isotherms fitted by Langmuir and Freundlich model of (c) g-C₃N₄ and (d) C₃N₅, respectively. q_e is the amount of dyes adsorbed at equilibrium while C_e is the equilibrium concentration of MB.

734 C₃N₅ from 664 to 680 nm is attributed to the transformation
 735 of MB into monomeric form and some degree of ground state
 736 charge transfer from C₃N₅ to MB during adsorption on the
 737 surface of C₃N₅. The dye adsorption performance of C₃N₅ was
 738 much higher than g-C₃N₄. MB is a well-known cationic dye
 739 possessing positive charge centered on the S atom in aqueous
 740 solutions.⁵⁸ On the other hand, the surface of C₃N₅ material
 741 has electron-rich character due to the presence of secondary N
 742 (NC₂) in heptazine moieties, terminal -NH₂ and π extended
 743 network. Therefore, electrostatic interactions between the
 744 positively charged MB molecule and negatively charged C₃N₅
 745 are likely responsible for the instantaneous adsorption.^{54,59} To
 746 confirm negative charge on the surface of C₃N₅, ζ -potential
 747 measurement was performed which depicts average surface
 748 charge of -36.2 mV and proves the electron-rich surface of
 749 C₃N₅ (Figure S8). Further, MB can also adsorb on the surface
 750 of C₃N₅ via π - π stacking between aromatic conjugated
 751 network of MB and π framework of C₃N₅ (Figure 9b).⁶⁰ To
 752 investigate the role of surface specific properties in the
 753 enhanced adsorption profile, Brunauer-Emmett-Teller
 754 (BET) surface area (S_{BET}), pore volume (V_p) and pore
 755 diameter (r_p) of g-C₃N₄ and C₃N₅ were measured by N₂
 756 adsorption and desorption. The obtained BET surface area,
 757 pore volume and pore diameter for g-C₃N₄ were found to be
 758 11.47 m² g⁻¹, 0.095 cm³ and 19.13 nm while these values for
 759 C₃N₅ were found to be 1.78 m² g⁻¹, 0.002 cm³ g⁻¹ and 16.98
 760 nm, respectively. The obtained surface values indicate a
 761 decrement in the surface area of C₃N₅ in comparison to g-
 762 C₃N₄. The relatively low surface area of C₃N₅ might be due to
 763 the less gas evolution (three NH₃ per heptazine unit) from
 764 melam hydrazine precursor during thermal annealing step

while the formation of g-C₃N₄ from melamine precursor 765
 releases six NH₃ molecule per heptazine unit. Further, 766
 hydrogen bonded melam hydrazine precursor might promote 767
 in-plane cross-linking of heptazine units leading to a stacked 768
 sheets type structure which reduces the effective accessible 769
 surface area. Contrarily, in g-C₃N₄ ring formation and 770
 polymerization step can produce cross-linking between sheets 771
 giving a porous structure with high surface area. The obtained 772
 results suggest that an electronic interaction between C₃N₅ and 773
 MB is responsible for the superior adsorption performance of 774
 C₃N₅ rather than an increased surface area. 775

To investigate whether the nature of adsorption was 776
 chemisorption or physisorption, and to explore the possibility 777
 of any chemical bonding, the C₃N₅/MB composite was 778
 analyzed using NMR spectroscopy. The ¹³C NMR spectrum 779
 of C₃N₅/MB composite did not show any change in peak 780
 position and intensity of C₃N₅, which demonstrated the 781
 adsorption of MB on C₃N₅ to be purely physisorptive in nature 782
 (Figure S9d). FTIR, Raman and PL spectra of C₃N₅/MB 783
 composite displayed various cumulative peaks and signals due 784
 to the presence of MB in the C₃N₅/MB composite. However, 785
 no evident signals for any chemical interaction can be 786
 identified, which further supports a purely physical interaction 787
 (physisorption) between C₃N₅ and MB (Figure S9a-c). 788
 Additionally, XPS spectra of C₃N₅/MB composite were 789
 identical to pristine C₃N₅ samples which revealed that C₃N₅ 790
 signals dominated over MB, and no change in BE value was 791
 observed which ruled out the possibility of any chemical bond 792
 formation between C₃N₅ and MB (Figure S10). 793

To quantify the excellent dye adsorption capacity of C₃N₅, 794
 various parameters such as the adsorption capacity, adsorption 795

Table 3. Pseudo-First- and Second-Order Kinetic Models of MB Adsorption on g-C₃N₄ and C₃N₅ and Langmuir and Freundlich Adsorption Models Showing Isotherm Constants

serial no.	sample name	pseudo-first-order			pseudo-second-order		
		k (s ⁻¹)	q_e (mg g ⁻¹)	R^2	k (s ⁻¹ mg ⁻¹ L)	q_e (mg g ⁻¹)	R^2
1	g-C ₃ N ₄	0.16	2.35	0.96	0.08	2.6	0.99
2	C ₃ N ₅	6.35	6.83	0.98	2.24	6.95	0.99
serial no.	sample name	Langmuir			Freundlich		
		Q (mg g ⁻¹)	b (L mg ⁻¹)	R^2	K (mg ¹⁻ⁿ L ⁿ g ⁻¹)	n	R^2
1.	g-C ₃ N ₄	6.03	0.13	0.97	1.21	0.43	0.96
2.	C ₃ N ₅	42.32	0.05	0.98	2.40	0.78	0.97

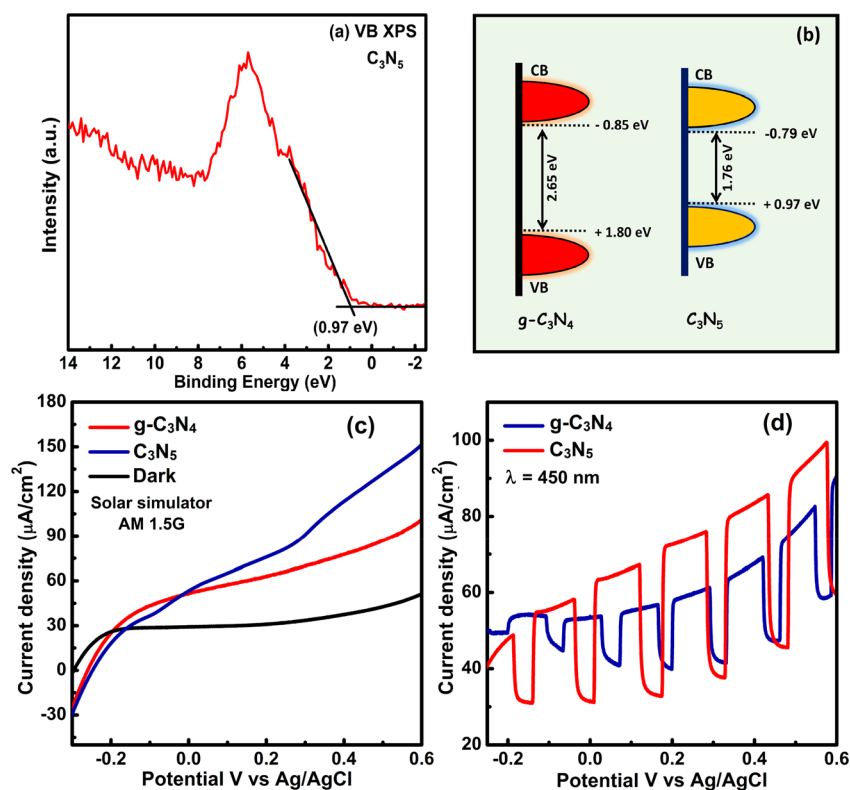


Figure 11. (a) XPS valence band spectra of C₃N₅ for determining energy levels. (b) Density of state revealing band structure of g-C₃N₄ and C₃N₅. (c) Linear sweep voltammogram showing current–potential characteristics of g-C₃N₄ (blue) and C₃N₅ (red) measured in 0.1 M Na₂SO₄ solution AM1.5G light irradiation (100 mW cm⁻²) and under dark conditions. (d) Light on–off showing photocurrent response vs applied voltage by using 450 nm wavelength light (54.15 mW cm⁻²) for g-C₃N₄ (blue) and C₃N₅ (red).

796 constants, linear regression correlation coefficient, and
 797 adsorption isotherm were measured and compared with
 798 pristine g-C₃N₄ (Figure 10 and Table 3). The adsorption
 799 capacity (amount of dye adsorbed) of g-C₃N₄ and MHP
 800 materials was calculated using eq 3:

$$801 \quad q = \frac{(C - C_e)V}{m} \quad (3)$$

802 Where q is the adsorption capacity, V is the volume of MB
 803 solution, m is the mass of the added adsorbent, and C and C_e
 804 are the initial and equilibrium concentrations of MB,
 805 respectively. The kinetics of methylene blue adsorption on
 806 the surface of g-C₃N₄ and C₃N₅ were investigated using first-
 807 and second-order adsorption kinetics using eqs 4 and 5:

$$808 \quad q_t = q_e(1 - e^{-kt}) \quad (4)$$

$$q_t = \frac{kq_e^2 t}{1 + kq_e t} \quad (5) \quad 809$$

Where q_e is adsorbed amount of dye after reaching equilibrium 810
 and q_t is the adsorbed amount at time t , and k is the pseudo- 811
 first-order or pseudo-second-order adsorption rate constant. 812
 The results obtained using pseudo-first-order and pseudo- 813
 second-order kinetics are displayed in Table 3 and Figure 814
 10a,b. The kinetic studies clearly demonstrate that the 815
 prepared C₃N₅ samples can reach approximately 95% 816
 adsorption–desorption equilibrium instantaneously (1 min), 817
 and complete adsorption–desorption equilibrium within 10 818
 min, which is an extraordinary performance compared to 819
 previously reported carbon nitride and carbon based materials 820
 which usually take 45 min to achieve equilibrium.⁶¹ In 821
 addition, the kinetics study indicated that the adsorption of 822
 methylene blue on the C₃N₅ and g-C₃N₄ materials follows 823
 pseudo-second-order adsorption kinetics, which agreed well 824

825 with previous reports.^{61a} For isotherm studies, standard
 826 solutions of 5, 10, 15, 20, 25 and 30 ppm MB in water were
 827 prepared; 50 mL of these standard solutions was placed in a
 828 beaker and 50 mg of the adsorbents was added to them. The
 829 solutions were kept under strong stirring for 30 min under dark
 830 conditions to reach equilibrium, and then the concentration of
 831 methylene blue was calculated using UV–vis spectroscopy (see
 832 Supporting Information for details). The adsorption isotherms
 833 of methylene blue were investigated in terms of the
 834 Langmuir^{61b,62} and Freundlich models^{61b,63} (eqs 6 and 7,
 835 respectively), and the results for g-C₃N₄ and C₃N₅ are
 836 displayed in Figure 10c,d, respectively; the relevant constants
 837 are reported in Table 3. It can be seen from Figure 10 and
 838 Table 3 that the value of R² extracted by employing the
 839 Langmuir isotherm model was higher than the R² value
 840 obtained from the Freundlich isotherm model, indicating that
 841 the Langmuir model representing complete monolayer cover-
 842 age on homogeneous sites was successful in predicting the
 843 adsorption of methylene blue on both g-C₃N₄ and C₃N₅.⁶⁴

$$844 \quad q_e = \frac{QbC_e}{(1 + bC_e)} \quad (6)$$

$$845 \quad q_e = KC_e^n \quad (7)$$

846 Where q_e is adsorbed amount of dye after reaching equilibrium
 847 (mg g⁻¹), R is correlation coefficient, Q is the monolayer
 848 adsorption capacity (mg g⁻¹), b is the adsorption coefficient (L
 849 mg⁻¹), C_e is the equilibrium concentration and K is the
 850 Freundlich constant.

851 To check whether C₃N₅ material displays any visible light
 852 induced dye degradation activity, 50 mL of 50 ppm MB
 853 containing solution was charged with 50 mg of C₃N₅ catalyst
 854 and stirred in the dark for 30 min to reach adsorption–
 855 desorption equilibrium. Subsequently, the obtained suspension
 856 was irradiated under simulated sunlight (AM1.5G, 100 mW
 857 cm⁻²). After every 10 min, 1 mL of sample was withdrawn and
 858 centrifuged to remove solid C₃N₅ and the supernatant liquid
 859 was analyzed with UV–vis spectroscopy. The UV–vis analysis
 860 indicated that the concentration of MB solution does not
 861 change even after 8 h of irradiation. These results suggest that
 862 C₃N₅ is not active for dye degradation, which might be because
 863 of unfavorable band alignment. To understand the band
 864 structure of C₃N₅, Mott–Schottky plots were obtained in 0.5
 865 M Na₂SO₄ solution (Figure S6b). From the Mott–Schottky
 866 plot, the flat band positions of g-C₃N₄ and C₃N₅ were found to
 867 be -1.05 and -0.91 V vs Ag/AgCl, respectively, which can be
 868 considered the conduction band position if the Fermi level lies
 869 just below conduction band (strong n -type character). Using
 870 the bandgap values obtained from the Tauc plot (2.65 eV for
 871 g-C₃N₄ and 1.76 eV for C₃N₅), the positions of the valence
 872 band edge for g-C₃N₄ and C₃N₅ were calculated to be +1.60
 873 and +0.85 V vs Ag/AgCl, respectively. Since the standard band
 874 edge positions are usually expressed with reference to NHE,
 875 the CB and VB positions of g-C₃N₄ were calculated to -0.85
 876 and +1.80 V vs NHE at pH 0, while CB and VB positions of
 877 C₃N₅ were found to be -0.72 and +1.04 V vs NHE at pH 0.

878 XPS valence band spectra of C₃N₅ was collected to get
 879 further information regarding the band structure (Figure 11a).
 880 The intersecting point obtained by extrapolation of XPS VB
 881 spectra on x and y axes gave the value of valence band
 882 maximum (VB_{max}). The VB_{max} of C₃N₅ was calculated to be
 883 +0.95 eV, which was approximately the same (+1.05 V)

obtained from the Mott–Schottky measurements and UV–vis 884
 data. Further, by using XPS VB and optical bandgap (1.76 eV) 885
 values, the CB_{min} and VB_{max} of C₃N₅ were calculated to be 886
 -0.79 and +0.97 eV, while for g-C₃N₄, CB_{min} and VB_{max} 887
 positions were found to be -0.85 and +1.80 eV, respectively. 888
 Figure 11b shows a schematic illustration of the density of 889
 states (DOS) distribution in C₃N₅ and g-C₃N₄. 890

The dye degradation process begins with the reaction with • 891
 OH radical originating from photogenerated holes in the 892
 valence band of the semiconductor. The oxidation potential of 893
 water to generate •OH radical (H₂O/•OH) is +2.38 V vs NHE 894
 at pH 0, which requires highly oxidative holes. Another route 895
 for the generation of •OH radicals is the reduction of O₂ to 896
 O₂^{•-} anion radical (O₂/O₂^{•-}, -0.33 V vs NHE at pH 0) at the 897
 conduction band followed by reaction with protons to afford • 898
 OH radicals.^{63,65} However, for this process required protons 899
 should be derived from water oxidation (H₂O/O₂, +1.23 V vs 900
 NHE at pH 0).^{64,66} Unfortunately, the valence band position 901
 of C₃N₅ is just +1.04 V vs NHE, which cannot facilitate water 902
 oxidation thus explaining the absence of photocatalytic activity 903
 for MB degradation. Nyquist plots of g-C₃N₄ and C₃N₅ 904
 determined with electrochemical impedance spectroscopy 905
 (EIS) under dark and AM1.5G irradiation demonstrate that 906
 the semicircle for C₃N₅ was larger than for g-C₃N₄, which 907
 represents a higher charge transfer resistance in C₃N₅ 908
 compared to g-C₃N₄; a higher charge carrier recombination 909
 is indicated in C₃N₅ (Figure S11). 910

Because of the unfavorable band edge positions of C₃N₅ 911
 (CB = -0.71 V and VB = +1.04 V vs NHE at pH 0), it is not 912
 able to function as a stand-alone catalyst for the photo- 913
 electrochemical splitting of water. However, the excellent 914
 visible light absorption of C₃N₅ encouraged us to investigate 915
 the photosensitizing effect of C₃N₅ to increase the photo- 916
 catalytic performance of TiO₂ (a wide bandgap semi- 917
 conductor).⁶⁷ The conduction band of C₃N₅ (-0.72 V vs 918
 NHE) was more negative than the conduction band of TiO₂ 919
 (-0.1 V vs NHE), which favors transfer of photogenerated 920
 electrons in the CB of C₃N₅ to the CB of TiO₂.⁶⁸ To measure 921
 photosensitizing performance, C₃N₅ and g-C₃N₄ powders were 922
 mixed with TiO₂ nanoparticles in α -terpineol solution (film- 923
 forming agent) followed by drop-casting on FTO:glass 924
 substrates coated with a thin (~ 50 nm) blocking layer of 925
 TiO₂. A three electrode setup consisting of the samples as the 926
 photoanode (working electrode), Pt as cathode (counter 927
 electrode) and Ag/AgCl reference electrode was used for 928
 photoelectrochemical water splitting experiments in 0.1 M 929
 Na₂SO₄ electrolyte, while a Class A solar simulator was used as 930
 the source of AM1.5G simulated sunlight (100 mW cm⁻²). 931
 Linear sweep voltammograms of electrodes consisting of C₃N₅ 932
 and pristine g-C₃N₄ samples mixed with TiO₂ NPs are shown 933
 in Figure 11a. It can be seen from Figure 11a that the 934
 photocurrent density for C₃N₅ sensitized TiO₂ was much 935
 higher than g-C₃N₄ sensitized TiO₂. The current density for 936
 C₃N₅ and g-C₃N₄ sample blended TiO₂ sample was found to 937
 be 152 and 100 μ A cm⁻² at an applied potential of +0.6 V vs 938
 NHE (or 1.23 V vs NHE). To probe the improved 939
 photosensitizing performance in the visible region, on–off 940
 experiments using a 450 nm LED (54.15 mW cm⁻²) were 941
 carried out, which clearly show the alternate drop and rise in 942
 photocurrents in on–off cycles (Figure 11b). Figure 11b also 943
 shows that the magnitude of the photocurrent was higher for 944
 the C₃N₅ sample. A similar pattern in the on–off cycle was 945
 observed when samples were irradiated with 505 nm LED 946

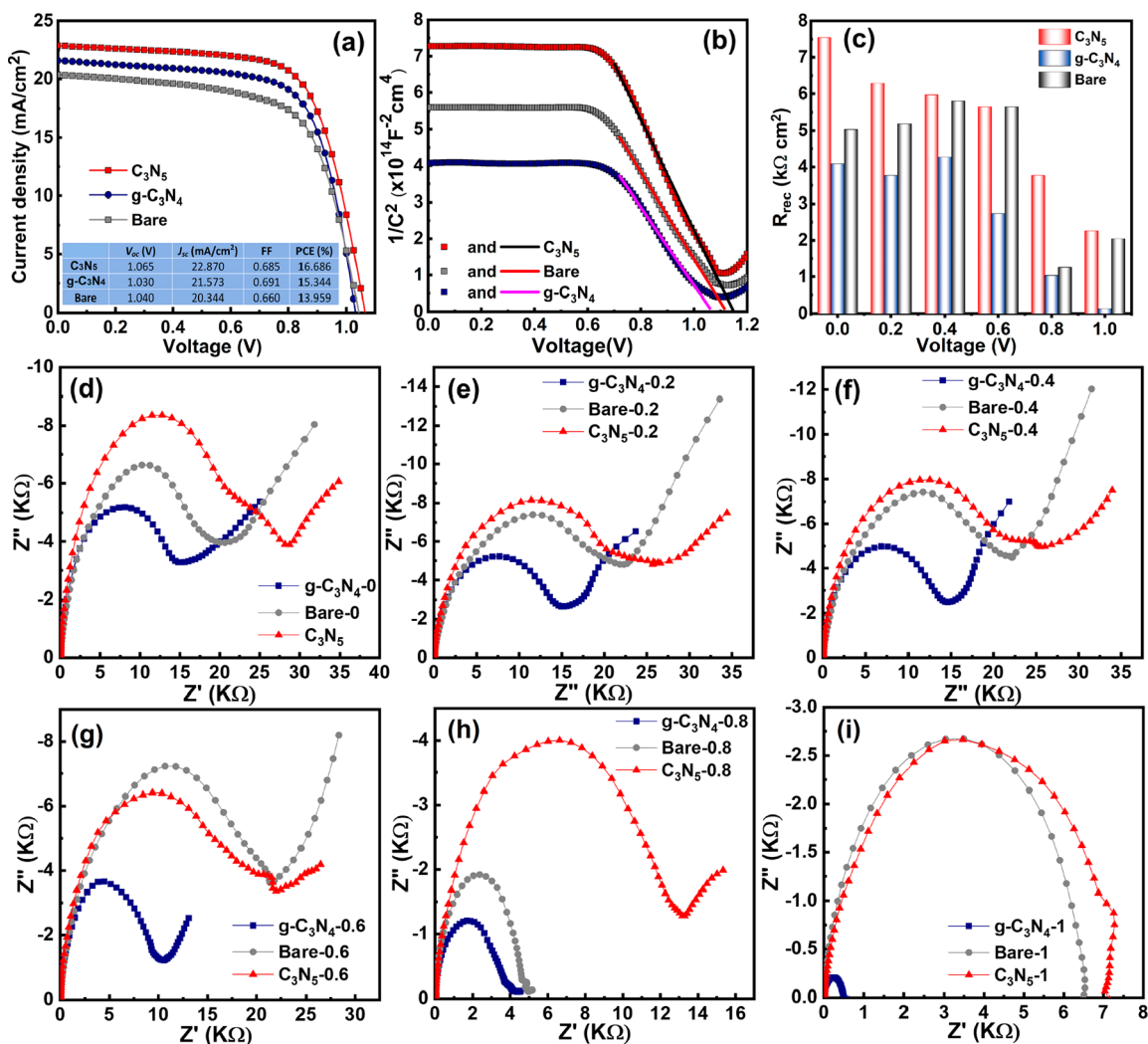


Figure 12. (a) Current–voltage characteristics of perovskite solar cells made with bare PbX₂, 4 wt % of g-C₃N₄ and C₃N₅ under AM1.5 G one sun illumination. (b) Mott–Schottky plot of the perovskite solar cells based on undoped and g-C₃N₄/C₃N₅-doped perovskite active layers. (c) Recombination resistance of perovskite solar cell based on undoped and doped Perovskite layer with CN and MHP in dark conditions. The corresponding equivalent circuit is shown in insets where R_s is series resistance, C is high-frequency capacitance, R is recombination resistance and Q is a constant phase element (CPE) with coefficient N. (d–i) Nyquist plots for perovskite solar cells made with bare PbX₂, g-C₃N₄ and C₃N₅ doping under dark conditions at 0.0, 0.2, 0.4, 0.6, 0.8 and 1.0 V.

947 (40.48 mW cm⁻²), confirming the improved photosensitizing
 948 properties of C₃N₅ at longer wavelengths (Figure S12).
 949 Further, photoelectrochemical water splitting experiment
 950 carried out using Na₂S (2.0 mmol) as hole scavenger showed
 951 enhanced photocurrent density, reaching up to 465 μA cm⁻²
 952 for C₃N₅ under AM 1.5 G irradiation (>420 nm) (Figure S13).
 953 Under identical conditions, the value of photocurrent density
 954 for g-C₃N₄ was found to be 373 μA cm⁻² (Figure S13a). A
 955 similar pattern was followed at higher wavelengths and
 956 calculated current density for C₃N₅ was found to be 454 and
 957 145 μA cm⁻² at 450 and 505 nm, while for g-C₃N₄ the value of
 958 current density was found to be 275 and 80 μA cm⁻²,
 959 respectively (Figure S13b). Photocurrent response of C₃N₅ as
 960 a function of time during light on–off cycle does not change
 961 significantly compared to g-C₃N₄, which demonstrates
 962 resiliency of C₃N₅ under reaction conditions and charge flow
 963 (Figure S14). The maximum applied bias photon-to-current
 964 efficiency (ABPE) and incident photon-to-current efficiency
 965 (IPCE) achieved by C₃N₅ was 0.059 and 2.33% (at 450 nm),

while the value for g-C₃N₄ was 0.048 and 1.41% (at 450 nm),
 respectively (Figure S13c,d).

To demonstrate the optoelectronic application of our newly
 synthesized graphenic semiconductor, we employed C₃N₅ as
 the electron transport layer (ETL) in MAPbBr₃ based
 perovskite solar cells and obtained a good result. Carbon
 based materials have frequently been used as hole transport
 layers (HTLs) or hole collection electrodes in MAPbBr₃ based
 solar cells, but have almost never been used (effectively) as
 ETLs to boost the open circuit photovoltage. Using C₃N₅ as
 the ETL and with no optimization of any kind, we measured a
 V_{oc} of 1.3 V, J_{sc} of 7.5 mA cm⁻² and a FF (fill factor) of 0.4 to
 obtain a power conversion efficiency (PCE) of 4.2% (Figures
 S15 and S16 in Supporting Information). Some context is
 needed to appreciate the significance of the aforementioned
 result. Methylammonium lead bromide (MAPbBr₃) is a halide
 perovskite with an electronic bandgap of 2.23 eV, which has
 two major advantages for solar cell applications in comparison
 to the more commonly used methylammonium lead iodide
 (MAPbI₃). In theory, it enables the construction of much

Table 4. Photovoltaic Performance of HPSCs Made with Bare PbX₂, 4 wt % g-C₃N₄ and C₃N₅ in PbX₂ Solution under AM1.5 G Solar Simulated Light

		V _{oc} (V)	J _{sc} (mA/cm ²)	FF	PCE (%)
C ₃ N ₅	maximum	1.065	22.870	0.685	16.686
	average	1.026 ± 0.043	22.560 ± 1.039	0.654 ± 0.044	15.142 ± 1.442
g-C ₃ N ₄	maximum	1.030	21.573	0.691	15.344
	average	0.984 ± 0.042	21.204 ± 0.565	0.670 ± 0.017	13.981 ± 0.949
bare	maximum	1.040	20.344	0.660	13.959
	average	1.041 ± 0.035	20.394 ± 0.200	0.647 ± 0.020	13.713 ± 0.245

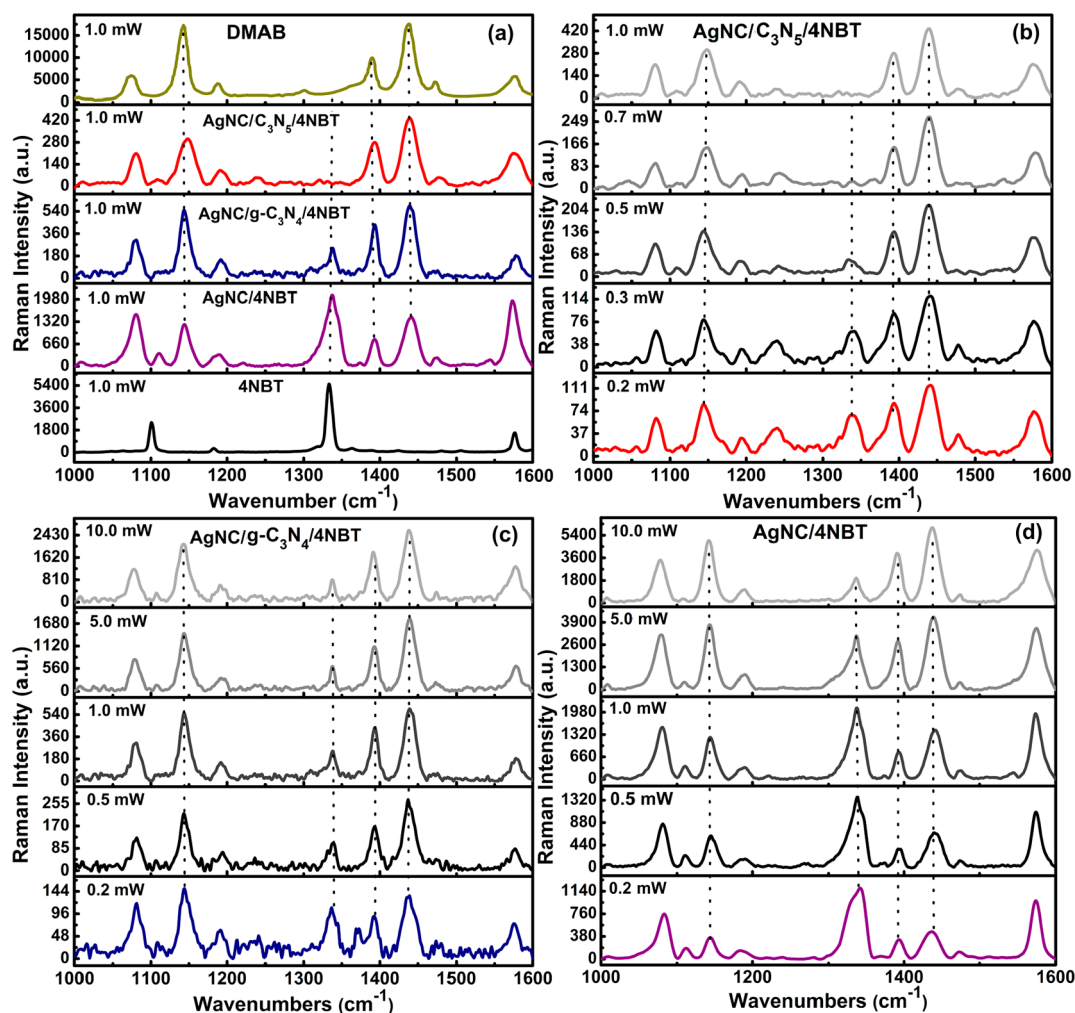


Figure 13. (a) Raman spectrum of pristine 4NBT (black), DMAB (yellow) and comparison of SERS spectra of plasmon-exciton coinduced surface catalytic reaction of 4NBT to DMAB on AgNC (purple), AgNC/g-C₃N₄ (blue) and AgNC/C₃N₅ (red) under 532 nm laser irradiation at 1.0 mW power and 60 s accumulation time and SERS spectra as a function of laser power for plasmon-exciton coinduced surface catalytic transformation of 4NBT to DMAB on (b) AgNC/C₃N₅ (c) AgNC/g-C₃N₄ and (d) AgNC. The gradual lightening of color as a function of laser power represents the transformation of 4NBT to DMAB.

986 higher V_{oc} solar cells that can be used to power electrocatalytic
 987 and electrochemical reactions and second, MAPbBr₃ is known
 988 to have superior ambient stability (less moisture sensitivity)
 989 and operational stability (due to the absence of phase
 990 transitions and enhanced thermal stability at a high working
 991 temperature) compared to MAPbI₃.⁶⁹ However, until recently,
 992 most works in this area failed to achieve the expected high V_{oc}
 993 value, and the typical V_{oc} values obtained using were in the
 994 range 0.90–1.16 V.⁷⁰ The use of carbon based charge transport
 995 layers has enabled a dramatic improvement in the performance
 996 of MAPbBr₃ based photovoltaic devices by generating

photovoltages in excess of 1.3 V (as high as 1.6 V) without
 suffering a corresponding penalty in the short circuit current
 (J_{sc}). The first such report was by Wu et al.⁷¹ wherein indene-
 C60 bisadduct (ICBA) was used as the acceptor in conjunction
 with MAPbBr₃ to realize a high V_{oc} perovskite solar cell.
 Shortly thereafter, Li et al. used carbon nanotubes as an
 efficient hole collector for MAPbBr₃ solar cells and achieved a
 V_{oc} of 1.4 V.⁷² MAPbBr₃ sandwiched between modified
 PEDOT:PSS (hole transport layer) and PC₆₁BM (electron
 transport layer) resulted in a solar cell with a V_{oc} of 1.52 V⁷³
 while a graphitic carbon anode (with no hole transport layer)

1008 and TiO₂ electron transport layer were used by Liang et al. to
1009 realize a MAPbBr₃ solar cell with a V_{oc} as high as 1.57 V.⁷⁴

1010 The origin of the poor V_{oc} values was poorly understood for
1011 a long time. Even now, there are two distinct explanations: one
1012 based on active layer material quality issues and another based
1013 on high interfacial recombination. For instance, vapor
1014 deposited MAPbBr₃ films were found to generate high V_{oc}
1015 values in comparison with solution-deposited films, which was
1016 attributed to the superior morphology and grain size in the
1017 vapor deposited films, and supported the explanation based
1018 invoking material quality.⁷⁵ The second explanation was
1019 supported by the observation of high V_{oc} values when hole
1020 transport layers with deep HOMO levels were used, indicating
1021 that the separation of the electron- and hole- quasi-Fermi levels
1022 at the charge extraction interfaces was the controlling
1023 mechanism determining V_{oc} .⁷⁶ Our examination of MAPbBr₃
1024 solar cells using C₃N₅ as the ETL provides a way to reconcile
1025 the above explanations. On the one hand, the high CB position
1026 of C₃N₅ is better aligned with the CB of MAPbBr₃, and enables
1027 an optimal value for the electron quasi-Fermi level at the
1028 perovskite–C₃N₅ interface. On the other hand, the low dark
1029 current observed using C₃N₅ ETL in comparison to both TiO₂
1030 and g-C₃N₄ ETLs (Figure S17 in Supporting Information)
1031 indicates suppression of trap-mediated hopping through
1032 MAPbBr₃ due to the insertion of C₃N₅ as a midgap state-
1033 free barrier layer, thus enabling the circumventing of active
1034 layer material quality issues. In summary, it is noteworthy that
1035 an unoptimized ETL made with a brand new semiconductor
1036 (C₃N₅) that was cast into films from a particulate suspension,
1037 generated a V_{oc} value of 1.3 V, higher than that generated by
1038 TiO₂ and g-C₃N₄ ETLs.

1039 The photovoltaic performance of halide perovskite solar cells
1040 is highly dependent on grain size and defects free lattice states
1041 and presence of small numbers of defects and trap sites have a
1042 detrimental effect. The trap assisted recombinations can be
1043 minimized by passivating perovskite layer with graphenic
1044 materials due to their high carrier mobility and surface area
1045 materials, which can efficiently capture charge and improve
1046 transportation behavior resulting in better photoconversion
1047 efficiency.⁷⁷ Further, incorporation of graphenic semiconduc-
1048 tors with perovskite precursor provide crystallization surface,
1049 which helps in increasing of grain size and minimize defects
1050 density at grain boundaries. The increased conjugation in C₃N₅
1051 should lead to electron-rich conductive surface with high
1052 charge carrier density and better carrier mobility than g-C₃N₄.
1053 To verify this assumption, we have blended MA_xFA_{1-x}Pb-
1054 (I_{0.85}Br_{0.15})₃ based perovskite with different wt % of C₃N₅ and
1055 g-C₃N₄. Under optimized conditions, 4 wt % doping of g-C₃N₄
1056 and C₃N₅ with respect to PbX₂ was found best performing and
1057 C₃N₅ outperformed over g-C₃N₄ and bare PbX₂ based solar
1058 cell architecture attributed to better charge separation in more
1059 conjugated C₃N₅ scaffold and reduced trap sites.

1060 Figure 12 shows the J – V curves of the best performing solar
1061 cells devices based on undoped and doped perovskite layers
1062 while the photovoltaic performance of solar cells is
1063 summarized in Table 4. Solar cells made with a compact
1064 undoped perovskite solar cell yielded a short circuit current
1065 density (J_{sc}) of about 20.344 mA/cm², an open circuit voltage
1066 (V_{oc}) of 1.04 V and fill factor (FF) of about 66% resulting in
1067 the overall power conversion efficiency (PCE) of about
1068 13.959%. While, perovskite solar cell made with g-C₃N₄-
1069 doped perovskite layer show a J_{sc} of 21.573 mA/cm², V_{oc} of
1070 1.03 V and fill factor of about 69.1% and corresponding PCE

of about 15.344%. C₃N₅-doped perovskite solar cells displayed
a PCE value of 16.689% resulting from V_{oc} of 1.065 V, J_{sc} of
22.87 mA/cm² and FF of 68.5%.

Capacitance–voltage measurement on fabricated devices
with doped/undoped perovskite layer was measured at 10 kHz
frequency in dark to determine bulk properties such as doping
density (N_D) and energy equilibrium at the contacts, which is
related to the flat-band potential (V_{fb}).⁷⁸ Mott–Schottky plots
for the devices made with doped and undoped perovskite layer
are shown in Figure 13.

$$\frac{1}{C_{sc}^2} = \frac{2}{e\epsilon_0\epsilon_r N_D} \left\{ (V - V_{fb}) - \frac{kT}{e} \right\} \quad (8)$$

$$N_D = \frac{2}{e\epsilon_0\epsilon_r n} \quad (9)$$

V_{fb} and N_D were calculated by using eq 8 and eq 9
respectively, where C_{sc} is the space-charge capacitance (i.e.,
film capacitance) per unit area; ϵ_r is the dielectric constant of
the material, ϵ_0 is the vacuum permittivity, k is Boltzmann
constant, T is temperature in Kelvin, e is the electron charge
and V is the applied potential. The measured V_{fb} of bare
undoped, g-C₃N₄-doped and C₃N₅-doped perovskite solar cell
was found to be 1.12, 1.08, and 1.15 V respectively, while
carrier concentration of the respective devices was found to be
 1.74×10^{16} , 1.96×10^{16} and 1.36×10^{16} cm⁻³. This proves
that doping perovskite layer with C₃N₅ significantly improves
the charge transport in the device compared to the undoped
and g-C₃N₄-doped devices.

To explore the charge transport characteristics, hole only
devices with the architecture of FTO/PEDOT:PSS/Perov-
skite/Spiro-oMeTAD/Au was measured by the space charge
limited current (SSLC) model described by the following
equation:

$$J = \frac{9}{8L^3} \epsilon_0 \epsilon_r \mu V^2 \quad (10)$$

Where ϵ_0 , ϵ_r , μ and L are permittivity of the free space, relative
permittivity of the perovskite, carrier mobility in the perovskite
layer and thickness of perovskite layer, respectively. The hole
mobility in pure perovskite was found to be 2.55×10^{-3} cm²/
sS, while that of g-C₃N₄- and C₃N₅-doped perovskite was
found to be 3.28×10^{-3} cm²/(V s) and 4.33×10^{-3} cm²/(V s),
respectively (Figure S19).

To get insight into the charge transfer properties of
perovskite solar cells based on undoped and doped perovskite
layer, solid-state impedance spectroscopy measurements in the
frequency range from 0.1 Hz to 1 MHz at different applied bias
under dark conditions were performed. The resulting Nyquist
plots were fitted with the circuit shown in inset of Figure 12c,
where R_s is series resistance, R_{rec} and C represent the resistance
and capacitance at the interface between the active layer and
charge transport layer and Q is a constant phase element
(CPE) with coefficient N . The resulting recombination
resistance of different solar cells obtained after fitting the
Nyquist plot observed from the low-frequency region at
different voltages is shown in Figure 12d–i. The C₃N₅-doped
device showed a higher value of R_{rec} compared to the g-C₃N₄-
doped and undoped devices. As the electron and hole
transporting layers for all kind of devices are same, the
difference in R_{rec} is mostly governed by the change in the
interfacial property of perovskite layer induced by doping with

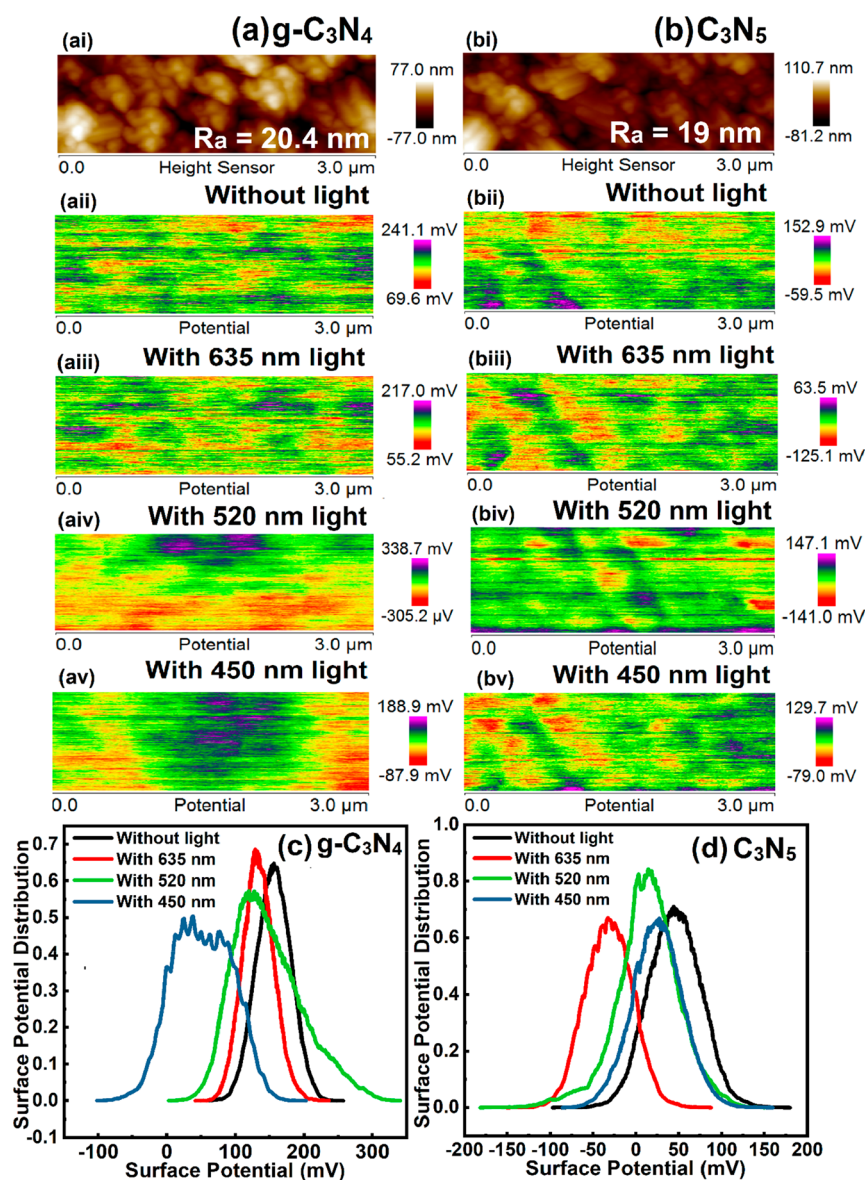


Figure 14. (a and b) Topographical AFM images (ai, bi) and Surface potential maps of $g\text{-C}_3\text{N}_4$ and C_3N_5 samples deposited on FTO (a ii and b ii) without light, (a iii and b iii) with 635 nm lased, (a iv and b iv) with 520 nm laser, (a v and b v) with 450 nm laser in sequence of top to bottom and surface potential distribution of (c) $g\text{-C}_3\text{N}_4$ and (d) C_3N_5 samples deposited on FTO under dark conditions, under illumination with 635, 520 and 450 nm laser.

C_3N_5 and $g\text{-C}_3\text{N}_4$. Interfacial recombination is inversely proportional to the recombination resistance; therefore, it can be concluded that the interfacial charge recombination in perovskite solar cells significantly gets suppressed by doping with MHP, while it increases by doping with $g\text{-C}_3\text{N}_4$ resulting in an improved V_{oc} in C_3N_5 based device followed by the undoped and doped devices.

The low band gap and extended π conjugation of C_3N_5 makes it an excellent candidate to harvest solar light to drive visible light induced catalytic reaction. Recently, plasmonic materials capable of generating hot electrons, coupled with graphenic materials, have shown wide potential in plasmon-exciton coinduced surface catalytic reactions.⁷⁹ The plasmon-exciton coupling for codriven chemical reactions can be measured by surface enhanced Raman spectroscopy (SERS).⁸⁰ To probe the viability C_3N_5 for promoting chemical reaction on its surface, the transformation of 4NBT (4-nitrobenzenethiol) to DMAB (4,4'-dimercaptoazobenzene) was chosen as

model reaction, while silver nanocubes (AgNC)⁸¹ were used as plasmonic material. The comparative SERS spectra of NBT adsorbed on bare AgNC , and AgNC decorated on $g\text{-C}_3\text{N}_4$ mW and C_3N_5 using 532 nm laser and 1 mW laser power are presented in Figure 13a. Normal Raman spectra of the pristine 4NBT powder show three main Raman signals at 1101, 1332 and 1576 cm^{-1} assigned to S—C stretch, NO_2 vibration and C=C stretch, respectively.⁸² After irradiating with 532 nm laser with a 1 mW power intensity, the N—O vibration was decreased and new peaks at 1142 (C—N stretch), 1389 and 1438 (N=N stretch) cm^{-1} corresponded to DMAB a_g modes emerged demonstrating conversion of 4NBT to DMAB.⁸³ For bare AgNC the drop in 4NBT peak was not significant, which showed inefficient surface-plasmon-to-hot-electron conversion to promote plasmon-driven chemical reaction. The $\text{AgNC}/g\text{-C}_3\text{N}_4$ showed a slight lowering of 4NBT peak intensity and rise in DMAB peaks; however, the peak was not disappeared suggesting incomplete transformation at lower laser power.

1163 While for AgNC/C₃N₅ the N—O vibration peak was
1164 completely disappeared at 1.0 mW laser power. Further, we
1165 tested laser power dependent SERS spectra on NBT adsorbed
1166 samples, which demonstrate complete disappearance of 4NBT
1167 peaks for Ag/C₃N₅ even at 0.7 mW, while bare Ag and AgNC/
1168 g-C₃N₄ system could not achieve complete degradation even at
1169 10 mW laser power (Figure 13b–d). Magnified SERS spectra
1170 of Ag/C₃N₅ in the 1270–1470 cm⁻¹ region showed a gradual
1171 decrease in N—O vibration peak as a function of laser power
1172 AgNC and completely disappeared at 1.0 mW (Figure S20). A
1173 sluggish transformation rate was observed for AgNC/g-C₃N₄
1174 and AgNC as evident from the increase in 4NBT peak at 1332
1175 cm⁻¹ along with DMAB peak at 1389 and 1438 cm⁻¹ as a
1176 function of laser intensity. The excellent conversion efficiency
1177 of AgNC/C₃N₅ assembly was attributed due to better
1178 plasmon-to-electron conversion efficiency on conjugated
1179 C₃N₅'s surface, which lead to high-density hot electrons to
1180 facilitate high catalytic conversion.^{79b}

1181 We performed thermogravimetric analysis (TGA) analysis of
1182 g-C₃N₄ samples to determine the thermal stability of materials
1183 (Figure S21). The TGA thermogram of g-C₃N₄ shows two
1184 weight loss regimes in the range of 60–150 °C and 500–740
1185 °C (Figure S21a). The first small weight loss (~6%) in the
1186 range of 60–150 °C was due to loss of surface adsorbed water
1187 molecules. The second major weight loss started from 550 °C,
1188 showed slow weight loss (~8%) up to 635 °C due to loss of
1189 NH₂ and condensation of heptazine units followed by almost
1190 ~70% sharp weight loss in the range of 635–740 °C due to
1191 degradation of heptazine moieties.⁸⁴ Following that, a steady
1192 weight loss was observed up to 900 °C due to the removal of
1193 residual carbon material. For C₃N₅, an initial small weight loss
1194 of 6% in the range of 60–150 °C was attributed due to loss of
1195 surface adsorbed and intercalated water (Figure S21b). A
1196 second steady weight loss (~34%) observed in the temperature
1197 range of 420–630 °C was assigned to loss of bridging azo
1198 nitrogens (–N=N–) and edge decorated –NH₂ nitrogens.

1199 The absence of any sharp weight loss for azo nitrogens
1200 demonstrates that azo nitrogens were not localized but present
1201 in a cross-linked heptazine network. Previous reports on azo-
1202 linked polymer also demonstrated excellent thermal stability of
1203 such polymers due to the formation of a rigid structure.⁸⁵
1204 Further, the observed weight loss value was in close agreement
1205 with expected weight loss value for azo nitrogen (33.5%)
1206 calculated by considering removal of three azo nitrogens
1207 (–N=N– shared by two heptazine) from azo-bridged C₆N₁₀
1208 unit, leaving behind C₆N₇ heptazine unit. These results further
1209 validated the presence of azo nitrogens in C₃N₅ polymer.
1210 Approximately 38% sharp weight loss in 630–720 °C region
1211 was assigned to degradation of heptazine ring system followed
1212 by slow weight loss up to 900 °C for residual carbon. Further,
1213 to investigate the nature of the product formed at high
1214 temperature, we annealed the sample in a closed evacuated
1215 quartz tube at 800 °C for 4 h. The orange product turned black
1216 and stuck to the wall of the tubes. Raman analysis of the
1217 product showed specific D, G band along with the 2D band
1218 and demonstrate its transformation into N-doped graphene/
1219 carbon (Figure S22). Previous reports also demonstrate the
1220 transformation of carbon nitride based materials/nitrogenous
1221 precursors into N-graphene/N-carbon at higher temperatures.

1222 To understand charge carrier dynamics and recombination
1223 mechanisms in C₃N₅, the surface potential changes of the
1224 samples under dark and under laser illumination at different
1225 wavelengths, were measured using Kelvin Probe Force

1226 Microscopy (KPFM) as illustrated in Figure 14. The surface
1227 topographical AFM image of g-C₃N₄ and C₃N₅ thin films
1228 deposited on bare FTO reveals an average roughness of 20.4
1229 and 19 nm, respectively (Figure 14ai,bi). Figure 14aii–v and
1230 bii–v displays the surface potential map of g-C₃N₄ and C₃N₅
1231 samples under dark conditions, 635, 520 and 450 nm,
1232 respectively. The FTO was grounded and behaves as an
1233 electron sink for photogenerated charges, leaving holes behind.
1234 The surface potential map under dark for both g-C₃N₄ and
1235 C₃N₅ shows even distribution of charge all over the surface of
1236 samples, (Figure 14aii,bii). After illumination with 635 nm
1237 laser the contrast of blue spots (positive potential shift) in the
1238 surface potential map was increased for both g-C₃N₄ and
1239 C₃N₅; however, this change was much intense for C₃N₅. Under
1240 520 nm light, the density of blue spots was slightly higher for g-
1241 C₃N₄ than C₃N₅, which drastically increased under 450 nm
1242 illumination (Figure 14a (aiv,v) and Figure 14b (biv,v)). These
1243 observations demonstrate that highest charge generation and
1244 accumulation on the surface was at 450 nm for g-C₃N₄ and at
1245 635 nm for C₃N₅ while remaining moderate for both at 520
1246 nm. Further, values of surface potential measured by KPFM
1247 under dark condition were found to be +156 and +45 mV for
1248 g-C₃N₄ and C₃N₅ respectively, which agreed well with the
1249 increased electron density on C₃N₅ than g-C₃N₄ due to
1250 contribution of charge from azo motif to heptazine ring system
1251 via extended orbital overlap (Figure 14c,d). The high surface
1252 negative charge of C₃N₅ was also confirmed by ζ-potential
1253 measurements (Figure S8). After illumination with 450 nm
1254 light, the surface potential was negatively shifted reaching
1255 maximum +40 mV for g-C₃N₄ and +25 mV for C₃N₅. Higher
1256 change in contact potential difference (CPD) or SP, i.e. 102
1257 mV, for g-C₃N₄ was observed due to good absorption at 450
1258 nm for generation of electron–hole pairs and accumulation of
1259 negative charge on the sample surface. The broad surface
1260 potential peaks and significantly larger CPD shift for g-C₃N₄
1261 were attributed possibly due to the longer lifetime (as
1262 confirmed by TRPL, Figure 8a) of g-C₃N₄ charge carriers
1263 resulting into delayed recombination of accumulated charge.
1264 Under 520 nm illumination, the surface potential values for g-
1265 C₃N₄ and C₃N₅ were measured to be 123 and 8 mV, while the
1266 change in SP was found to be 33 and 37 mV, respectively. For
1267 g-C₃N₄, relatively small CPD shifting at 520 nm can be
1268 explained due to its limited absorption at 520 nm wavelength
1269 generating fewer numbers of excitons, while in C₃N₅ most of
1270 the photogenerated charge get recombined due to faster
1271 recombination rate. Interestingly, C₃N₅ showed an unusually
1272 high SP shift (77 mV) at 635 nm, while g-C₃N₄ showed an
1273 explicitly small CPD shift (30 mV). The exceptional high SP
1274 shift at 635 nm demonstrated azo motif plays a certain role in
1275 charge carrier generation and stabilization at a longer
1276 wavelength. Azo-bridged aromatic compounds are well-
1277 known for their visible light absorption due to the presence
1278 of azo chromophore (–N=N–) in conjugation with aromatic
1279 units. The n–π* transition corresponding to azo nitrogen
1280 nonbonding orbital to the π* orbital of conjugated nitrogens in
1281 azo moiety occurs at low energy giving visible light
1282 absorption.⁸⁶ In C₃N₅ where electron withdrawing heptazine
1283 units (C₆H₇) were bridged together with azo bonds, these low
1284 energy transition can take place at 635 nm resulting into
1285 increase CPD shift at 635 nm. The high surface potential of
1286 C₃N₅ at 635 nm validates its potential to generate excitons at
1287 longer wavelengths.

1288 ■ CONCLUSION

1289 We report the synthesis of a modified carbon nitride
1290 framework C_3N_5 polymer containing exceptionally high N:C
1291 atomic ratio (5:3) melem hydrazine as the monomeric unit.
1292 Extensive characterization of C_3N_5 with XPS, EELS, NMR
1293 spectroscopy and elemental analysis suggested the presence of
1294 heptazine moiety bridged by azo nitrogens in the C_3N_5
1295 framework. Because of the overlap between the π orbitals of
1296 azo-bridged units and the π -conjugated network of the
1297 heptazine unit, the bandgap of C_3N_5 material was significantly
1298 reduced which, in turn, enabled optical absorption extended up
1299 to 700 nm and a bandgap of 1.76 eV. The position of the
1300 valence band in C_3N_5 was raised (+1.04 V vs NHE) in
1301 comparison to g- C_3N_4 (+1.80 V vs NHE) and C_3N_5 displayed
1302 excellent photosensitizing behavior to sensitize TiO_2 at longer
1303 wavelengths (505 nm) to facilitate photoelectrochemical water
1304 splitting. Because of the increased nitrogen content and the
1305 availability of electron-rich basic nitrogen sites, C_3N_5 materials
1306 displayed astonishing dye adsorption performance for methyl-
1307 ene blue removal reaching 90% adsorption–desorption
1308 equilibria within 1 min and complete adsorption–desorption
1309 equilibria within 10 min. In conjunction with Ag nanocubes,
1310 C_3N_5 displayed excellent photocatalytic activity for the
1311 plasmon-exciton (plexciton) codriven reduction of 4-nitro-
1312 benzenethiol to 4,4'-dimercaptoazobenzene. A prototypical
1313 solar cell device using C_3N_5 ETL and MAPbBr₃ displayed an
1314 improved V_{oc} of 1.3 V and power conversion efficiency (PCE)
1315 of 4.2% higher than g- C_3N_4 ETL. C_3N_5 blended with
1316 MA_xFA_{1-x}Pb(I_{0.85}Br_{0.15})₃ perovskite active layer achieved a
1317 photoconversion efficiency (PCE) as high as 16.7%.

1318 ■ ASSOCIATED CONTENT

1319 ● Supporting Information

1320 The Supporting Information is available free of charge on the
1321 ACS Publications website at DOI: 10.1021/jacs.9b00144.

1322 Experimental details, chemical structures, Supporting
1323 Figures (Figure S1–S22), XPS, ssNMR, Raman, electro-
1324 chemical characterization (Mott–Schottky, EIS), PL,
1325 fluorescence lifetime imaging, ζ -potential, EELS, TGA,
1326 photoelectrochemical water splitting results (under AM
1327 1.5G irradiation, LEDs PCE, IPCE, APCE, $i-t$ curve),
1328 solar cell results ($J-V$ curves, action spectra) and
1329 plexitonic performance (SERS spectra) (PDF)

1330 ■ AUTHOR INFORMATION

1331 Corresponding Authors

1332 *pawan@ualberta.ca

1333 *kshankar@ualberta.ca

1334 ORCID

1335 Pawan Kumar: 0000-0003-2804-9298

1336 Guy M. Bernard: 0000-0003-1507-6705

1337 Vladimir K. Michaelis: 0000-0002-6708-7660

1338 Karthik Shankar: 0000-0001-7347-3333

1339 Notes

1340 The authors declare no competing financial interest.

1341 ■ ACKNOWLEDGMENTS

1342 We thank the Natural Sciences and Engineering Research
1343 Council of Canada (NSERC), the National Research Council
1344 Canada (NRC), Future Energy Systems (FES) and CMC
1345 Microsystems for direct and indirect (equipment use) financial

support. U.K.T. is supported by a graduate student scholarship 1346
from Alberta Innovates. Some device fabrication and testing 1347
used research infrastructure made possible by a Leaders 1348
Opportunity Fund grant to K.S. from the Canada Foundation 1349
for Innovation and the Alberta Small Equipment Grants 1350
Program. We acknowledge use of the following facilities: the 1351
National Research Council - National Institute for Nano- 1352
technology (NRC-NINT) Electron Microscopy Lab, the Cell 1353
Imaging Facility, the Analytical Chemistry Laboratory and the 1354
University of Alberta Nanofab. Drs. Shihong Xu and Wayne 1355
Moffat are kindly acknowledged for assisting in He-ion 1356
imaging, CHNS elemental analysis, respectively. We thank 1357
Prof. Alkiviathes Meldrum for allowing the use of his lab to 1358
perform PL lifetime measurements. 1359

1360 ■ REFERENCES

- (1) (a) Brabec, C. J.; Winder, C.; Sariciftci, N. S.; Hummelen, J. C.; 1361
Dhanabalan, A.; van Hal, P. A.; Janssen, R. A. *Adv. Funct. Mater.* **2002**, 1362
12, 709–712. (b) Kim, J.-S.; Lu, L.; Sreearunothai, P.; Seeley, A.; Yim, 1363
K.-H.; Petrozza, A.; Murphy, C. E.; Beljonne, D.; Cornil, J.; Friend, R. 1364
H. *J. Am. Chem. Soc.* **2008**, 130, 13120–13131. (c) Liang, Y. Y.; Yu, L. 1365
P. *Acc. Chem. Res.* **2010**, 43, 1227–1236. (d) Bandara, J.; Shankar, K.; 1366
Grimes, C. A.; Thelakkat, M. *Thin Solid Films* **2011**, 520, 582–590. 1367
(e) Baeg, K. J.; Caironi, M.; Noh, Y. Y. *Adv. Mater.* **2013**, 25, 4210– 1368
4244. (f) Hu, X. W.; Dong, Y.; Huang, F.; Gong, X.; Cao, Y. J. *J. Phys.* 1369
Chem. C **2013**, 117, 6537–6543. (g) Scaccabarozzi, A.; Stingelin, N. J. 1370
J. Mater. Chem. A **2014**, 2, 10818–10824. (h) Fokina, A.; Lee, Y.; 1371
Chang, J. H.; Park, M.; Sung, Y.; Bae, W. K.; Char, K.; Lee, C.; Zentel, 1372
R. *Adv. Mater. Interfaces* **2016**, 3, 1600279. (i) Gao, L.; Zhang, Z. G.; 1373
Bin, H.; Xue, L.; Yang, Y.; Wang, C.; Liu, F.; Russell, T. P.; Li, Y. *Adv.* 1374
Mater. **2016**, 28, 8288–8295. (j) Mola, G. T.; Dlamini, W. E.; Oseni, 1375
S. O. *J. Mater. Sci.: Mater. Electron.* **2016**, 27, 11628–11633. 1376
(k) Chang, P.-H.; Tsai, Y.-C.; Shen, S.-W.; Liu, S.-Y.; Huang, K.-Y.; 1377
Li, C.-S.; Chang, H.-P.; Wu, C.-I. *ACS Photonics* **2017**, 4, 2335–2344. 1378
(l) Schroeder, B. C.; Kurosawa, T.; Fu, T. R.; Chiu, Y. C.; Mun, J.; 1379
Wang, G. J. N.; Gu, X. D.; Shaw, L.; Kneller, J. W. E.; Kreouzis, T.; 1380
Toney, M. F.; Bao, Z. A. *Adv. Funct. Mater.* **2017**, 27, 1701973. 1381
(m) Zhao, W.; Li, S.; Zhang, S.; Liu, X.; Hou, J. *Adv. Mater.* **2017**, 29, 1382
1604059. (n) Kang, M. J.; Khim, D.; Kim, J.; Lee, H. J.; Jo, J. Y.; Baeg, 1383
K. J.; Kim, D. Y. *Org. Electron.* **2018**, 58, 12–17. (o) Brabec, C. J.; 1384
Winder, C.; Sariciftci, N. S.; Hummelen, J. C.; Dhanabalan, A.; van 1385
Hal, P. A.; Janssen, R. A. *J. Adv. Funct. Mater.* **2002**, 12, 709–712. 1386
(p) Kim, J. S.; Lu, L.; Sreearunothai, P.; Seeley, A.; Yim, K. H.; 1387
Petrozza, A.; Murphy, C. E.; Beljonne, D.; Cornil, J.; Friend, R. H. *J.* 1388
Am. Chem. Soc. **2008**, 130, 13120–13131. (q) Bandara, J.; Shankar, 1389
K.; Grimes, C. A.; Thelakkat, M. *Thin Solid Films* **2011**, 520, 582– 1390
590. (r) Scaccabarozzi, A. D.; Stingelin, N. J. *J. Mater. Chem. A* **2014**, 1391
2, 10818–10824. (s) Gao, L.; Zhang, Z. G.; Bin, H. J.; Xue, L. W.; 1392
Yang, Y. K.; Wang, C.; Liu, F.; Russell, T. P.; Li, Y. *J. Adv. Mater.* 1393
2016, 28, 8288–8295. (t) Chang, P. H.; Tsai, Y. C.; Shen, S. W.; Liu, 1394
S. Y.; Huang, K. Y.; Li, C. S.; Chang, H. P.; Wu, C. I. *ACS Photonics* 1395
2017, 4, 2335–2344. (u) Zhong, L.; Gao, L.; Bin, H. J.; Hu, Q.; 1396
Zhang, Z. G.; Liu, F.; Russell, T. P.; Zhang, Z. J.; Li, Y. *Energy* 1397
Mater. **2017**, 7, 1602215. 1398
(2) Po, R.; Bianchi, G.; Carbonera, C.; Pellegrino, A. *Macromolecules* 1399
2015, 48, 453–461. 1400
(3) (a) Di Pietro, R.; Fazzi, D.; Kehoe, T. B.; Siringhaus, H. *J. Am.* 1401
Chem. Soc. **2012**, 134, 14877–14889. (b) Chen, C. Y.; Tsao, C. S.; 1402
Huang, Y. C.; Liu, H. W.; Chiu, W. Y.; Chuang, C. M.; Jeng, U. S.; Su, 1403
C. J.; Wu, W. R.; Su, W. F.; Wang, L. *Nanoscale* **2013**, 5, 7629–7638. 1404
(c) Phan, H.; Wang, M.; Bazan, G. C.; Nguyen, T. Q. *Adv. Mater.* 1405
2015, 27, 7004–7009. (d) Ye, Z.; Cui, H.; Yang, X.; Qiu, F. *J. Mater.* 1406
Chem. C **2015**, 3, 1949–1956. (e) Pearson, A. J.; Hopkinson, P. E.; 1407
Couderc, E.; Domanski, K.; Abdi-Jalebi, M.; Greenham, N. C. *Org.* 1408
Electron. **2016**, 30, 225–236. (f) Hsieh, Y. J.; Huang, Y. C.; Liu, W. S.; 1409
Su, Y. A.; Tsao, C. S.; Rwei, S. P.; Wang, L. *ACS Appl. Mater. Interfaces* 1410
2017, 9, 14808–14816. (g) Un, H. I.; Zheng, Y. Q.; Shi, K.; Wang, J. 1411

- 1412 Y.; Pei, J. *Adv. Funct. Mater.* **2017**, *27*, 1605058. (h) Di Pietro, R.;
1413 Fazzi, D.; Kehoe, T. B.; Sirringhaus, H. *J. Am. Chem. Soc.* **2012**, *134*,
1414 14877–14889. (i) Kim, S. H.; Yoon, W. M.; Jang, M.; Yang, H.; Park,
1415 J. J.; Park, C. E. *J. Mater. Chem.* **2012**, *22*, 7731–7738. (j) Phan, H.;
1416 Wang, M.; Bazan, G. C.; Nguyen, T. Q. *Adv. Mater.* **2015**, *27*, 7004–
1417 7004. (k) Ye, Z.; Cui, H. N.; Yang, X. B.; Qiu, F. *J. Mater. Chem. C*
1418 **2015**, *3*, 1949–1956. (l) Pearson, A. J.; Hopkinson, P. E.; Couderc,
1419 E.; Domanski, K.; Abdi-Jalebi, M.; Greenham, N. C. *Org. Electron.*
1420 **2016**, *30*, 225–236. (m) Un, H. I.; Zheng, Y. Q.; Shi, K.; Wang, J. Y.;
1421 Pei, J. *Adv. Funct. Mater.* **2017**, *27*, 1605058.
1422 (4) (a) Matthews, J. R.; Niu, W. J.; Tandia, A.; Wallace, A. L.; Hu, J.
1423 Y.; Lee, W. Y.; Giri, G.; Mannsfeld, S. C. B.; Xie, Y. T.; Cai, S. C.;
1424 Fong, H. H.; Bao, Z. N.; He, M. Q. *Chem. Mater.* **2013**, *25*, 782–789.
1425 (b) Marzano, G.; Ciasca, C. V.; Babudri, F.; Bianchi, G.; Pellegrino,
1426 A.; Po, R.; Farinola, G. M. *Eur. J. Org. Chem.* **2014**, *2014*, 6583–6614.
1427 (c) Bohra, H.; Wang, M. F. *J. Mater. Chem. A* **2017**, *5*, 11550–11571.
1428 (5) (a) Zhang, X. M.; Wang, A. Z.; Zhao, M. W. *Carbon* **2015**, *84*,
1429 1–8. (b) Berger, D.; Ratsch, C. *Phys. Rev. B: Condens. Matter Mater.*
1430 *Phys.* **2016**, *93*, 235441.
1431 (6) (a) Kumar, P.; Boukherroub, R.; Shankar, K. J. *J. Mater. Chem. A*
1432 **2018**, *6*, 12876–12931. (b) Linley, S.; Liu, Y.; Ptacek, C. J.; Blowes,
1433 D. W.; Gu, F. X. *ACS Appl. Mater. Interfaces* **2014**, *6*, 4658–4668.
1434 (c) Putz, M. V.; Buzatu, D. L.; Mirica, M. C.; Ori, O. *Fullerenes*,
1435 *Nanotubes, Carbon Nanostruct.* **2018**, *26*, 303–314.
1436 (7) (a) Sridharan, K.; Kuriaakose, T.; Philip, R.; Park, T. J. *Appl. Surf.*
1437 *Sci.* **2014**, *308*, 139–147. (b) Liu, J.; Liu, Y.; Liu, N.; Han, Y.; Zhang,
1438 X.; Huang, H.; Lifshitz, Y.; Lee, S.-T.; Zhong, J.; Kang, Z. *Science*
1439 **2015**, *347*, 970. (c) Kumar, P.; Thakur, U. K.; Alam, K.; Kar, P.;
1440 Kisslinger, R.; Zeng, S.; Patel, S.; Shankar, K. *Carbon* **2018**, *137*, 174–
1441 187.
1442 (8) Wen, J.; Xie, J.; Chen, X.; Li, X. *Appl. Surf. Sci.* **2017**, *391*, 72–
1443 123.
1444 (9) (a) Zhou, Z.; Zhang, Y.; Shen, Y.; Liu, S.; Zhang, Y. *Chem. Soc.*
1445 *Rev.* **2018**, *47*, 2298–2321. (b) Ong, W.-J.; Tan, L.-L.; Ng, Y. H.;
1446 Yong, S.-T.; Chai, S.-P. *Chem. Rev.* **2016**, *116*, 7159–7329. (c) Zheng,
1447 Y.; Lin, L.; Wang, B.; Wang, X. *Angew. Chem., Int. Ed.* **2015**, *54*,
1448 12868–12884.
1449 (10) (a) Cao, S.; Low, J.; Yu, J.; Jaroniec, M. *Adv. Mater.* **2015**, *27*,
1450 2150–2176. (b) Wang, Y.; Wang, X.; Antonietti, M. *Angew. Chem.,*
1451 *Int. Ed.* **2012**, *51*, 68–89. (c) Wang, Y.; Zhang, J.; Wang, X.;
1452 Antonietti, M.; Li, H. *Angew. Chem., Int. Ed.* **2010**, *49*, 3356–3359.
1453 (11) (a) Zhang, Y.; Mori, T.; Ye, J.; Antonietti, M. *J. Am. Chem. Soc.*
1454 **2010**, *132*, 6294–6295. (b) Hong, J.; Xia, X.; Wang, Y.; Xu, R. *J.*
1455 *Mater. Chem.* **2012**, *22*, 15006–15012. (c) Wang, Y.; Di, Y.;
1456 Antonietti, M.; Li, H.; Chen, X.; Wang, X. *Chem. Mater.* **2010**, *22*,
1457 5119–5121. (d) Ran, J.; Ma, T. Y.; Gao, G.; Du, X.-W.; Qiao, S. Z.
1458 *Energy Environ. Sci.* **2015**, *8*, 3708–3717. (e) Lin, J.; Pan, Z.; Wang, X.
1459 *ACS Sustainable Chem. Eng.* **2014**, *2*, 353–358. (f) Wang, Y.; Li, H.;
1460 Yao, J.; Wang, X.; Antonietti, M. *Chem. Sci.* **2011**, *2*, 446–450.
1461 (12) (a) Yang, S.; Gong, Y.; Zhang, J.; Zhan, L.; Ma, L.; Fang, Z.;
1462 Vajtai, R.; Wang, X.; Ajayan, P. M. *Adv. Mater.* **2013**, *25*, 2452–2456.
1463 (b) Kumar, A.; Kumar, P.; Joshi, C.; Ponnada, S.; Pathak, A. K.; Ali,
1464 A.; Sreedhar, B.; Jain, S. L. *Green Chem.* **2016**, *18*, 2514–2521.
1465 (c) Kumar, A.; Kumar, P.; Pathak, A. K.; Chokkapu, A. N.; Jain, S. L.
1466 *ChemistrySelect* **2017**, *2*, 3437–3443.
1467 (13) Mane, G. P.; Talapaneni, S. N.; Lakhi, K. S.; Ilbeygi, H.; Ravon,
1468 U.; Al-Bahily, K.; Mori, T.; Park, D. H.; Vinu, A. *Angew. Chem., Int.*
1469 *Ed.* **2017**, *56*, 8481–8485.
1470 (14) (a) Mane, G. P.; Dhawale, D. S.; Anand, C.; Ariga, K.; Ji, Q.;
1471 Wahab, M. A.; Mori, T.; Vinu, A. *J. Mater. Chem. A* **2013**, *1*, 2913–
1472 2920. (b) Talapaneni, S. N.; Mane, G. P.; Park, D.-H.; Lakhi, K. S.;
1473 Ramadass, K.; Joseph, S.; Skinner, W. M.; Ravon, U.; Al-Bahily, K.;
1474 Vinu, A. *J. Mater. Chem. A* **2017**, *5*, 18183–18192. (c) Talapaneni, S.
1475 N.; Mane, G. P.; Mano, A.; Anand, C.; Dhawale, D. S.; Mori, T.; Vinu,
1476 A. *ChemSusChem* **2012**, *5*, 700–708. (d) Lakhi, K. S.; Park, D.-H.; Al-
1477 Bahily, K.; Cha, W.; Viswanathan, B.; Choy, J.-H.; Vinu, A. *Chem. Soc.*
1478 *Rev.* **2017**, *46*, 72–101.
(15) Kim, I. Y.; Kim, S.; Jin, X.; Premkumar, S.; Chandra, G.; Lee, 1479
N.-S.; Mane, G. P.; Hwang, S.-J.; Umapathy, S.; Vinu, A. *Angew.* 1480
Chem. **2018**, *130*, 17381–17386. 1481
(16) Fang, J.; Fan, H.; Li, M.; Long, C. *J. Mater. Chem. A* **2015**, *3*, 1482
13819–13826. 1483
(17) Zhang, P.; Li, X.; Shao, C.; Liu, Y. *J. Mater. Chem. A* **2015**, *3*, 1484
3281–3284. 1485
(18) (a) Jürgens, B.; Irran, E.; Senker, J.; Kroll, P.; Müller, H.; 1486
Schnick, W. *J. Am. Chem. Soc.* **2003**, *125*, 10288–10300. (b) Chu, S.; 1487
Wang, C.; Feng, J.; Wang, Y.; Zou, Z. *Int. J. Hydrogen Energy* **2014**, *39*, 1488
13519–13526. (c) Saplinova, T.; Lehnert, C.; Böhme, U.; Wagler, J.; 1489
Kroke, E. *New J. Chem.* **2010**, *34*, 1893–1908. (d) Chu, S.; Wang, Y.; 1490
Guo, Y.; Feng, J.; Wang, C.; Luo, W.; Fan, X.; Zou, Z. *ACS Catal.* 1491
2013, *3*, 912–919. 1492
(19) Shiraiishi, Y.; Kanazawa, S.; Kofuji, Y.; Sakamoto, H.; Ichikawa, 1493
S.; Tanaka, S.; Hirai, T. *Angew. Chem., Int. Ed.* **2014**, *53*, 13454– 1494
13459. 1495
(20) Che, W.; Cheng, W.; Yao, T.; Tang, F.; Liu, W.; Su, H.; Huang, 1496
Y.; Liu, Q.; Liu, J.; Hu, F.; et al. *J. Am. Chem. Soc.* **2017**, *139*, 3021– 1497
3026. 1498
(21) (a) Miller, D. R.; Swenson, D. C.; Gillan, E. G. *J. Am. Chem.* 1499
Soc. **2004**, *126*, 5372–5373. (b) Miller, D. R.; Holst, J. R.; Gillan, E. 1500
Inorg. Chem. **2007**, *46*, 2767–2774. 1501
(22) Gillan, E. G. *Chem. Mater.* **2000**, *12*, 3906–3912. 1502
(23) (a) Saplinova, T.; Bakumov, V.; Gmeiner, T.; Wagler, J.; 1503
Schwarz, M.; Kroke, E. *Z. Z. Anorg. Allg. Chem.* **2009**, *635*, 2480– 1504
2487. (b) Sattler, A.; Schönberger, S.; Schnick, W. *Z. Z. Anorg. Allg.* 1505
Chem. **2010**, *636*, 476–482. 1506
(24) Makowski, S. J.; Köstler, P.; Schnick, W. *Chem. - Eur. J.* **2012**, 1507
18, 3248–3257. 1508
(25) (a) Kumar, A.; Kumar, P.; Borkar, R.; Bansiwala, A.; Labhsetwar, 1509
N.; Jain, S. L. *Carbon* **2017**, *123*, 371–379. (b) Yu, H.; Shi, R.; Zhao, 1510
Y.; Bian, T.; Zhao, Y.; Zhou, C.; Waterhouse, G. I.; Wu, L. Z.; Tung, 1511
C. H.; Zhang, T. *Adv. Mater.* **2017**, *29*, 1605148. 1512
(26) (a) Xia, P.; Zhu, B.; Yu, J.; Cao, S.; Jaroniec, M. *J. Mater. Chem.* 1513
A **2017**, *5*, 3230–3238. (b) Mao, J.; Peng, T.; Zhang, X.; Li, K.; Ye, 1514
L.; Zan, L. *Catal. Sci. Technol.* **2013**, *3*, 1253–1260. 1515
(27) Axen, N.; Botton, G.; Somekh, R.; Hutchings, I. *Diamond Relat.* 1516
Mater. **1996**, *5*, 163–168. 1517
(28) Hu, J.; Yang, P.; Lieber, C. M. *Phys. Rev. B: Condens. Matter* 1518
Mater. Phys. **1998**, *57*, R3185. 1519
(29) Li, X.; Zhang, J.; Shen, L.; Ma, Y.; Lei, W.; Cui, Q.; Zou, G. 1520
Appl. Phys. A: Mater. Sci. Process. **2009**, *94*, 387–392. 1521
(30) Seyfarth, L.; Senker, J. *Phys. Chem. Chem. Phys.* **2009**, *11*, 1522
3522–3531. 1523
(31) (a) Sehnert, J.; Baerwinkel, K.; Senker, J. *J. Phys. Chem. B* **2007**, 1524
111, 10671–10680. (b) Hu, Y.; Shim, Y.; Oh, J.; Park, S.; Park, S.; 1525
Ishii, Y. *Chem. Mater.* **2017**, *29*, 5080–5089. 1526
(32) Cui, Y.; Ding, Z.; Fu, X.; Wang, X. *Angew. Chem., Int. Ed.* **2012**, 1527
51, 11814–11818. 1528
(33) Sattler, A.; Pagano, S.; Zeuner, M.; Zurawski, A.; Gunzelmann, 1529
D.; Senker, J.; Müller-Buschbaum, K.; Schnick, W. *Chem. - Eur. J.* 1530
2009, *15*, 13161–13170. 1531
(34) (a) Hsu, C.-Y.; Chang, K.-S. *J. Phys. Chem. C* **2018**, *122*, 3506– 1532
3512. (b) Rovnyak, D.; Baldus, M.; Itin, B. A.; Bennati, M.; Stevens, 1533
A.; Griffin, R. G. *J. Phys. Chem. B* **2000**, *104*, 9817–9822. 1534
(35) Lotsch, B. V.; Schnick, W. *Chem. - Eur. J.* **2007**, *13*, 4956–4968. 1535
(36) Guo, Q.; Zhang, Y.; Qiu, J.; Dong, G. *J. Mater. Chem. C* **2016**, 1536
4, 6839–6847. 1537
(37) (a) Gulaczyk, I.; Kręglewski, M.; Valentin, A. *J. Mol. Spectrosc.* 1538
2003, *220*, 132–136. (b) Dirtu, D.; Odochian, L.; Pui, A.; 1539
Humelnicu, I. *Open Chem.* **2006**, *4*, 666–673. 1540
(38) (a) Niu, P.; Zhang, L.; Liu, G.; Cheng, H. M. *Adv. Funct. Mater.* 1541
2012, *22*, 4763–4770. (b) Xu, J.; Zhang, L.; Shi, R.; Zhu, Y. *J. Mater.* 1542
Chem. A **2013**, *1*, 14766–14772. 1543
(39) (a) Zheng, H.; Chen, W.; Gao, H.; Wang, Y.; Guo, H.; Guo, S.; 1544
Tang, Z.; Zhang, J. *J. Mater. Chem. C* **2017**, *5*, 10746–10753. (b) Lau, 1545
V. W.-h.; Mesch, M. B.; Duppel, V.; Blum, V.; Senker, J. r.; Lotsch, B. 1546
V. J. Am. Chem. Soc. **2015**, *137*, 1064–1072. 1547

- 1548 (40) (a) Wang, X.; Maeda, K.; Thomas, A.; Takanabe, K.; Xin, G.;
1549 Carlsson, J. M.; Domen, K.; Antonietti, M. *Nat. Mater.* **2009**, *8*, 76.
1550 (b) Bojdys, M. J.; Müller, J. O.; Antonietti, M.; Thomas, A. *Chem. -*
1551 *Eur. J.* **2008**, *14*, 8177–8182.
- 1552 (41) Kroke, E.; Schwarz, M.; Horath-Bordon, E.; Kroll, P.; Noll, B.;
1553 Norman, A. D. *New J. Chem.* **2002**, *26*, 508–512.
- 1554 (42) Tonda, S.; Kumar, S.; Kandula, S.; Shanker, V. *J. Mater. Chem.*
1555 *A* **2014**, *2*, 6772–6780.
- 1556 (43) Jiang, J.; Ou-yang, L.; Zhu, L.; Zheng, A.; Zou, J.; Yi, X.; Tang,
1557 H. *Carbon* **2014**, *80*, 213–221.
- 1558 (44) Cui, Y.; Zhang, J.; Zhang, G.; Huang, J.; Liu, P.; Antonietti, M.;
1559 Wang, X. *J. Mater. Chem.* **2011**, *21*, 13032–13039.
- 1560 (45) Zhang, J.; Zhang, M.; Lin, S.; Fu, X.; Wang, X. *J. Catal.* **2014**,
1561 *310*, 24–30.
- 1562 (46) (a) Sharma, P.; Sasson, Y. *Green Chem.* **2017**, *19*, 844–852.
1563 (b) Yuan, B.; Chu, Z.; Li, G.; Jiang, Z.; Hu, T.; Wang, Q.; Wang, C. *J.*
1564 *Mater. Chem. C* **2014**, *2*, 8212–8215.
- 1565 (47) Zhang, G.; Zhang, M.; Ye, X.; Qiu, X.; Lin, S.; Wang, X. *Adv.*
1566 *Mater.* **2014**, *26*, 805–809.
- 1567 (48) (a) Shalom, M.; Inal, S.; Fettkenhauer, C.; Neher, D.;
1568 Antonietti, M. *J. Am. Chem. Soc.* **2013**, *135*, 7118–7121. (b) Shalom,
1569 M.; Guttentag, M.; Fettkenhauer, C.; Inal, S.; Neher, D.; Llobet, A.;
1570 Antonietti, M. *Chem. Mater.* **2014**, *26*, 5812–5818.
- 1571 (49) (a) Kang, Y.; Yang, Y.; Yin, L. C.; Kang, X.; Wang, L.; Liu, G.;
1572 Cheng, H. M. *Adv. Mater.* **2016**, *28*, 6471–6477. (b) Yang, P.; Ou,
1573 H.; Fang, Y.; Wang, X. *Angew. Chem., Int. Ed.* **2017**, *56*, 3992–3996.
- 1574 (50) Alibart, F.; Lejeune, M.; Durand Drouhin, O.; Zellama, K.;
1575 Benlahsen, M. *J. Appl. Phys.* **2010**, *108*, No. 053504.
- 1576 (51) (a) Zhang, Y.; Pan, Q.; Chai, G.; Liang, M.; Dong, G.; Zhang,
1577 Q.; Qiu, J. *Sci. Rep.* **2013**, *3*, 1943. (b) Sun, C.; Tay, B.; Lau, S.; Sun,
1578 X.; Zeng, X.; Li, S.; Bai, H.; Liu, H.; Liu, Z.; Jiang, E. *J. Appl. Phys.*
1579 **2001**, *90*, 2615–2617.
- 1580 (52) Niu, P.; Liu, G.; Cheng, H.-M. *J. Phys. Chem. C* **2012**, *116*,
1581 11013–11018.
- 1582 (53) (a) Chen, L. C.; Teng, C. Y.; Lin, C. Y.; Chang, H. Y.; Chen, S.
1583 J.; Teng, H. *Adv. Energy Mater.* **2016**, *6*, 1600719. (b) Yeh, T. F.;
1584 Teng, C. Y.; Chen, S. J.; Teng, H. *Adv. Mater.* **2014**, *26*, 3297–3303.
1585 (c) Yeh, T.-F.; Chen, S.-J.; Yeh, C.-S.; Teng, H. *J. Phys. Chem. C* **2013**,
1586 *117*, 6516–6524. (d) Shi, R.; Li, Z.; Yu, H.; Shang, L.; Zhou, C.;
1587 Waterhouse, G. I.; Wu, L. Z.; Zhang, T. *ChemSusChem* **2017**, *10*,
1588 4650–4656. (e) Chen, L. C.; Teng, C. Y.; Lin, C. Y.; Chang, H. Y.;
1589 Chen, S. J.; Teng, H. *Adv. Energy Mater.* **2016**, *6*, 1600719. (f) Shi, R.;
1590 Li, Z.; Yu, H.; Shang, L.; Zhou, C.; Waterhouse, G. I. N.; Wu, L.-Z.;
1591 Zhang, T. *ChemSusChem* **2017**, *10*, 4650–4656.
- 1592 (54) Liang, Q.; Li, Z.; Huang, Z. H.; Kang, F.; Yang, Q. H. *Adv.*
1593 *Funct. Mater.* **2015**, *25*, 6885–6892.
- 1594 (55) (a) Sun, J.; Zhang, J.; Zhang, M.; Antonietti, M.; Fu, X.; Wang,
1595 X. *Nat. Commun.* **2012**, *3*, 1139. (b) Liu, Q.; Chen, T.; Guo, Y.;
1596 Zhang, Z.; Fang, X. *Appl. Catal., B* **2016**, *193*, 248–258. (c) Ye, X.;
1597 Cui, Y.; Wang, X. *ChemSusChem* **2014**, *7*, 738–742.
- 1598 (56) (a) Chen, Z.; Sun, P.; Fan, B.; Liu, Q.; Zhang, Z.; Fang, X.
1599 *Appl. Catal., B* **2015**, *170*, 10–16. (b) Zhang, M.; Duan, Y.; Jia, H.;
1600 Wang, F.; Wang, L.; Su, Z.; Wang, C. *Catal. Sci. Technol.* **2017**, *7*,
1601 452–458.
- 1602 (57) (a) Qin, J.; Wang, S.; Ren, H.; Hou, Y.; Wang, X. *Appl. Catal., B*
1603 **2015**, *179*, 1–8. (b) Luo, L.; Zhang, M.; Wang, P.; Wang, Y.; Wang,
1604 F. *New J. Chem.* **2018**, *42*, 1087–1091.
- 1605 (58) Ali, H. *Water, Air, Soil Pollut.* **2010**, *213*, 251–273.
- 1606 (59) Mittal, A.; Mittal, J.; Malviya, A.; Kaur, D.; Gupta, V. *J. Colloid*
1607 *Interface Sci.* **2010**, *343*, 463–473.
- 1608 (60) Yagub, M. T.; Sen, T. K.; Afroze, S.; Ang, H. M. *Adv. Colloid*
1609 *Interface Sci.* **2014**, *209*, 172–184.
- 1610 (61) (a) Fronczak, M.; Krajewska, M.; Demby, K.; Bystrzejewski, M.
1611 *J. Phys. Chem. C* **2017**, *121*, 15756–15766. (b) Zhu, B.; Xia, P.; Ho,
1612 W.; Yu, J. *Appl. Surf. Sci.* **2015**, *344*, 188–195.
- 1613 (62) Langmuir, I. *J. Am. Chem. Soc.* **1918**, *40*, 1361–1403.
- 1614 (63) Freundlich, H. *J. Phys. Chem.* **1906**, *57*, 1100–1107.
- 1615 (64) Han, S.; Liu, K.; Hu, L.; Teng, F.; Yu, P.; Zhu, Y. *Sci. Rep.* **2017**,
1616 *7*, 43599.
- (65) Gaya, U. I.; Abdullah, A. H. *J. Photochem. Photobiol., C* **2008**, *9*, 1617
1–12.
- (66) Ahmad, H.; Kamarudin, S.; Minggu, L.; Kassim, M. *Renewable*
1619 *Sustainable Energy Rev.* **2015**, *43*, 599–610.
- (67) Pelaez, M.; Nolan, N. T.; Pillai, S. C.; Seery, M. K.; Falaras, P.;
1621 Kontos, A. G.; Dunlop, P. S.; Hamilton, J. W.; Byrne, J. A.; O’shea, K.;
1622 et al. *Appl. Catal., B* **2012**, *125*, 331–349.
- (68) Zhou, X.; Peng, F.; Wang, H.; Yu, H.; Fang, Y. *Chem. Commun.* **2011**,
1624 *47*, 10323–10325.
- (69) (a) Zheng, X. J.; Chen, B.; Yang, M. J.; Wu, C. C.; Orler, B.;
1626 Moore, R. B.; Zhu, K.; Priya, S. *ACS Energy Lett.* **2016**, *1*, 424–430.
1627 (b) Askar, A. M.; Bernard, G. M.; Wiltshire, B.; Shankar, K.;
1628 Michaelis, V. K. *J. Phys. Chem. C* **2017**, *121*, 1013–1024.
- (70) Zhao, Y.; Nardes, A. M.; Zhu, K. *Faraday Discuss.* **2014**, *176*, 1630
1631 301–312.
- (71) Wu, C. G.; Chiang, C. H.; Chang, S. H. *Nanoscale* **2016**, *8*, 1632
1633 4077–4085.
- (72) Li, Z.; Boix, P. P.; Xing, G. C.; Fu, K. W.; Kulkarni, S. A.;
1634 Batabyal, S. K.; Xu, W. J.; Cao, A. Y.; Sum, T. C.; Mathews, N.; Wong,
1635 L. H. *Nanoscale* **2016**, *8*, 6352–6360.
- (73) Zuo, C. T.; Ding, L. M. *Adv. Energy Mater.* **2017**, *7*, 1601193.
- (74) Liang, Y. Q.; Wang, Y. J.; Mu, C.; Wang, S.; Wang, X. N.; Xu,
1638 D. S.; Sun, L. C. *Adv. Energy Mater.* **2018**, *8*, 1701159.
- (75) Sheng, R.; Ho-Baillie, A.; Huang, S. J.; Chen, S.; Wen, X. M.;
1640 Hao, X. J.; Green, M. A. *J. Phys. Chem. C* **2015**, *119*, 3545–3549.
- (76) Ryu, S.; Noh, J. H.; Jeon, N. J.; Kim, Y. C.; Yang, S.; Seo, J. W.;
1642 Seok, S. I. *Energy Environ. Sci.* **2014**, *7*, 2614–2618.
- (77) (a) Chen, X.; Liu, Q.; Wu, Q.; Du, P.; Zhu, J.; Dai, S.; Yang, S.
1644 *Adv. Funct. Mater.* **2016**, *26*, 1719–1728. (b) He, M.; Chen, Y.; Liu,
1645 H.; Wang, J.; Fang, X.; Liang, Z. *Chem. Commun.* **2015**, *51*, 9659–
1646 9661. (c) Zhu, Z.; Ma, J.; Wang, Z.; Mu, C.; Fan, Z.; Du, L.; Bai, Y.;
1647 Fan, L.; Yan, H.; Phillips, D. L.; et al. *J. Am. Chem. Soc.* **2014**, *136*,
1648 3760–3763. (d) Hadadian, M.; Correa-Baena, J. P.; Goharshadi, E.
1649 K.; Ummadisingu, A.; Seo, J. Y.; Luo, J.; Gholipour, S.; Zakeeruddin,
1650 S. M.; Saliba, M.; Abate, A.; et al. *Adv. Mater.* **2016**, *28*, 8681–8686.
- (e) Jiang, L. L.; Wang, Z. K.; Li, M.; Zhang, C. C.; Ye, Q. Q.; Hu, K.
1652 H.; Lu, D. Z.; Fang, P. F.; Liao, L. S. *Adv. Funct. Mater.* **2018**, *28*,
1653 1705875.
- (78) (a) Kirchartz, T.; Gong, W.; Hawks, S. A.; Agostinelli, T.;
1655 MacKenzie, R. C. I.; Yang, Y.; Nelson, J. J. *J. Phys. Chem. C* **2012**, *116*,
1656 7672–7680. (b) Guo, X.; Tan, Q.; Liu, S.; Qin, D.; Mo, Y.; Hou, L.;
1657 Liu, A.; Wu, H.; Ma, Y. *Nano Energy* **2018**, *46*, 150–157. (c) Liu, Z.;
1658 Zhu, A.; Cai, F.; Tao, L.; Zhou, Y.; Zhao, Z.; Chen, Q.; Cheng, Y.-B.;
1659 Zhou, H. *J. Mater. Chem. A* **2017**, *5*, 6597–6605. (d) Liu, Z.; Chang,
1660 J.; Lin, Z.; Zhou, L.; Yang, Z.; Chen, D.; Zhang, C.; Liu, S.; Hao, Y. **1661**
1662 *Adv. Energy Mater.* **2018**, *8*, 1703432. (e) Jahandar, M.; Heo, J. H.;
1663 Song, C. E.; Kong, K.-J.; Shin, W. S.; Lee, J.-C.; Im, S. H.; Moon, S.-J.
1664 *Nano Energy* **2016**, *27*, 330–339. (f) He, Q.; Yao, K.; Wang, X.; Xia,
1665 X.; Leng, S.; Li, F. *ACS Appl. Mater. Interfaces* **2017**, *9*, 41887–41897.
- (g) Niu, G.; Wang, S.; Li, J.; Li, W.; Wang, L. *J. Mater. Chem. A* **2018**,
1666 *6*, 4721–4728.
- (79) (a) Lin, W.; Cao, E.; Zhang, L.; Xu, X.; Song, Y.; Liang, W.;
1668 Sun, M. *Nanoscale* **2018**, *10*, 5482–5488. (b) Kang, L.; Chu, J.; Zhao,
1669 H.; Xu, P.; Sun, M. *J. Mater. Chem. C* **2015**, *3*, 9024–9037. (c) Ding,
1670 Q.; Shi, Y.; Chen, M.; Li, H.; Yang, X.; Qu, Y.; Liang, W.; Sun, M. *Sci.*
1671 *Rep.* **2016**, *6*, 32724. (d) Wu, H. Y.; Lai, Y. H.; Hsieh, M. S.; Lin, S.
1672 D.; Li, Y. C.; Lin, T. W. *Adv. Mater. Interfaces* **2014**, *1*, 1400119.
- (80) (a) Liang, X.; You, T.; Liu, D.; Lang, X.; Tan, E.; Shi, J.; Yin, P.;
1674 Guo, L. *Phys. Chem. Chem. Phys.* **2015**, *17*, 10176–10181. (b) Zhao,
1675 J.; Sun, M.; Liu, Z.; Quan, B.; Gu, C.; Li, J. *Sci. Rep.* **2015**, *5*, 16019.
1676 (81) Siekkinen, A. R.; McLellan, J. M.; Chen, J.; Xia, Y. *Chem. Phys.*
1677 *Lett.* **2006**, *432*, 491–496.
- (82) Dong, B.; Fang, Y.; Xia, L.; Xu, H.; Sun, M. *J. Raman Spectrosc.* **2011**,
1680 *42*, 1205–1206.
- (83) (a) Canpean, V.; Iosin, M.; Astilean, S. *Chem. Phys. Lett.* **2010**,
1681 *500*, 277–282. (b) Fang, Y.; Li, Y.; Xu, H.; Sun, M. *Langmuir* **2010**,
1682 *26*, 7737–7746.

- 1684 (84) (a) Kang, Y.; Yang, Y.; Yin, L. C.; Kang, X.; Liu, G.; Cheng, H.
1685 *M. Adv. Mater.* **2015**, *27*, 4572–4577. (b) Niu, P.; Qiao, M.; Li, Y.;
1686 Huang, L.; Zhai, T. *Nano Energy* **2018**, *44*, 73–81.
1687 (85) (a) Dang, Q.-Q.; Wang, X.-M.; Zhan, Y.-F.; Zhang, X.-M.
1688 *Polym. Chem.* **2016**, *7*, 643–647. (b) Patel, H. A.; Je, S. H.; Park, J.;
1689 Chen, D. P.; Jung, Y.; Yavuz, C. T.; Coskun, A. *Nat. Commun.* **2013**,
1690 *4*, 1357. (c) Patel, H. A.; Je, S. H.; Park, J.; Jung, Y.; Coskun, A.;
1691 Yavuz, C. T. *Chem. - Eur. J.* **2014**, *20*, 772–780.
1692 (86) (a) Clark, M. *Handbook of textile and industrial dyeing:*
1693 *principles, processes and types of dyes*; Elsevier: 2011. (b) Zollinger, H.
1694 *Color chemistry: syntheses, properties, and applications of organic dyes*
1695 *and pigments*; John Wiley & Sons: 2003. (c) Robin, M. B.; Simpson,
1696 W. T. *J. J. Chem. Phys.* **1962**, *36*, 580–588.